

Visual Decoding and Reconstruction via EEG Embeddings with Guided Diffusion

Dongyang Li^{1*}, Chen Wei^{1*}, Shiying Li¹, Jiachen Zou¹, and Quanying Liu^{1†}

¹Department of Biomedical Engineering, Southern University of Science and Technology, Shenzhen, China

{lidy2023, weic3}@mail.sustech.edu.cn,
liuqy@sustech.edu.cn

Abstract. How to decode human vision through neural signals has attracted a long-standing interest in neuroscience and machine learning. Modern contrastive learning and generative models improved the performance of fMRI-based visual decoding and reconstruction. However, the high cost and low temporal resolution of fMRI limit their applications in brain-computer interfaces (BCIs), prompting a high need for EEG-based visual reconstruction. In this study, we present an EEG-based visual reconstruction framework. It consists of a plug-and-play *EEG encoder* called the Adaptive Thinking Mapper (ATM), which is aligned with image embeddings, and a two-stage *EEG guidance image generator* that first transforms EEG features into image priors and then reconstructs the visual stimuli with a pre-trained image generator. Our approach allows EEG embeddings to achieve superior performance in image classification and retrieval tasks. Our two-stage image generation strategy vividly reconstructs images seen by humans. Furthermore, we analyzed the impact of signals from different time windows and brain regions on decoding and reconstruction. The versatility of our framework is demonstrated in the magnetoencephalogram (MEG) data modality. We report that EEG-based visual decoding achieves SOTA performance, highlighting the portability, low cost, and high temporal resolution of EEG, enabling a wide range of BCI applications. Our code is available at https://github.com/dongyangli-del/EEG_Image_decode.

Keywords: EEG · Visual reconstruction · Neural alignment · MEG

1 Introduction

A key technical challenge in brain-computer interfaces (BCIs) is to decode/reconstruct the visual world seen by humans through non-invasive brain recordings, such as functional magnetic resonance imaging (fMRI), magnetoencephalography (MEG) or electroencephalography (EEG). These highly dynamic brain activities reflect human perception of the visual world, which is influenced by properties of the external visual stimulus, our internal states, emotions and even personal experiences. Thus, visual decoding and reconstruction based on neural signals can uncover how the human brain processes and interprets natural visual stimuli, as well as promote non-invasive BCI applications.

Contrastive learning and generative models have greatly advanced fMRI-based visual decoding in both decoding tasks (e.g., image classification and retrieval) and generative tasks

* D. Li and C. Wei contributed equally.

† Corresponding author.

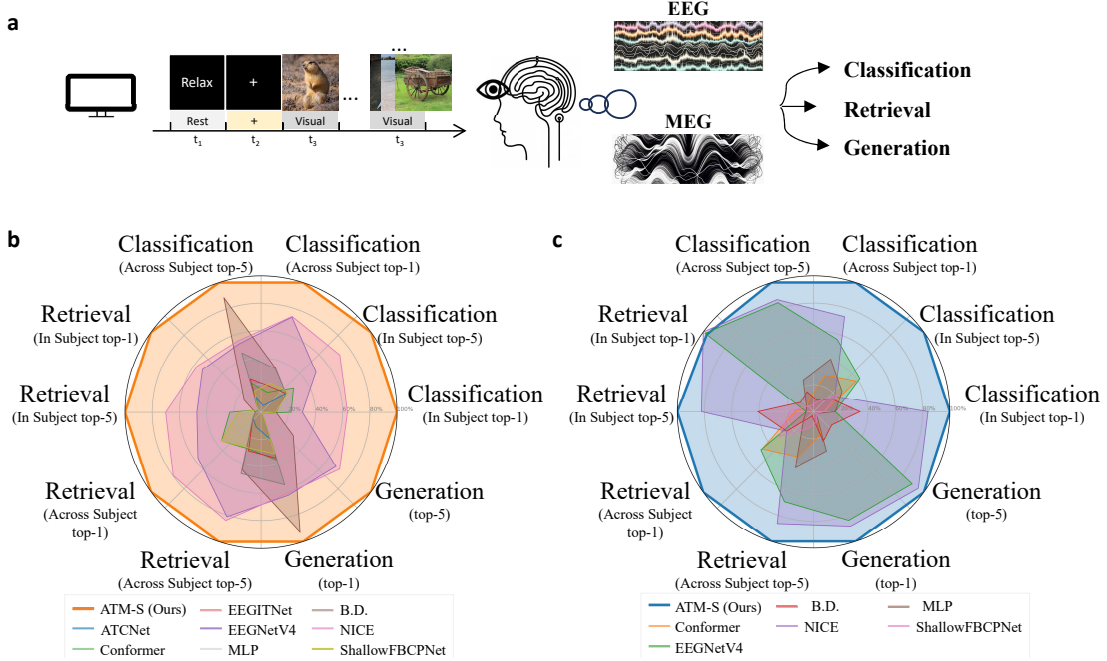


Fig. 1. EEG/MEG-based visual retrieval, classification, and reconstruction tasks. (a) Overview of three visual decoding tasks using EEG/MEG data under natural image stimuli. (b) Comparisons of nine encoders on the THINGS-EEG dataset, including within-subject and cross-subject performance. (c) Comparisons on the THINGS-MEG dataset, similar to (b). Our ATM-S encoder achieves the highest performance compared to other competing encoders in EEG/MEG-based visual decoding tasks.

(e.g., image reconstruction). By combining pre-trained visual models, existing fMRI decoding models can learn highly-refined feature embeddings in limited data [28, 40]. Using these embedded fMRI features, generative models such as diffusion models can reconstruct the image one is seeing [40, 12]. However, despite many advances in fMRI-based visual decoding, fMRI equipment is unportable, expensive, and difficult to operate, largely limiting its application in BCIs. Alternatively, EEG is portable, cheap, and universal, facilitating a wide range of BCI applications. EEG has higher temporal resolution and can effectively capture rapid changes in brain activity when processing complex, dynamic visual stimuli.

However, EEG has long been considered incomparable to fMRI in natural image decoding/reconstruction tasks, as EEG suffers from low signal-to-noise ratio, low spatial resolution, and large inter-subject variability. Recent advances in multimodal alignment have made MEG/EEG visual decoding possible, although the performance is still inferior to fMRI [8, 46, 16]. Yohann Benchetrit et al. used the CLIP model to extract the latent representation of the image and trained the MEG encoder to align it with the image representation extracted by CLIP. It achieved excellent retrieval and reconstruction performance on MEG and fMRI datasets, demonstrating the potential for real-time visual decoding and reconstruction using EEG/MEG signals. Recently, Song et al. [46] used an EEG encoder based on ShallowNet [37] and performed representation alignment through contrastive learning, achieving excellent decoding performance on the THING-EEG dataset [14]. These two studies provide preliminary evidence of the potential of EEG/MEG-based visual decoding. However, there is a significant

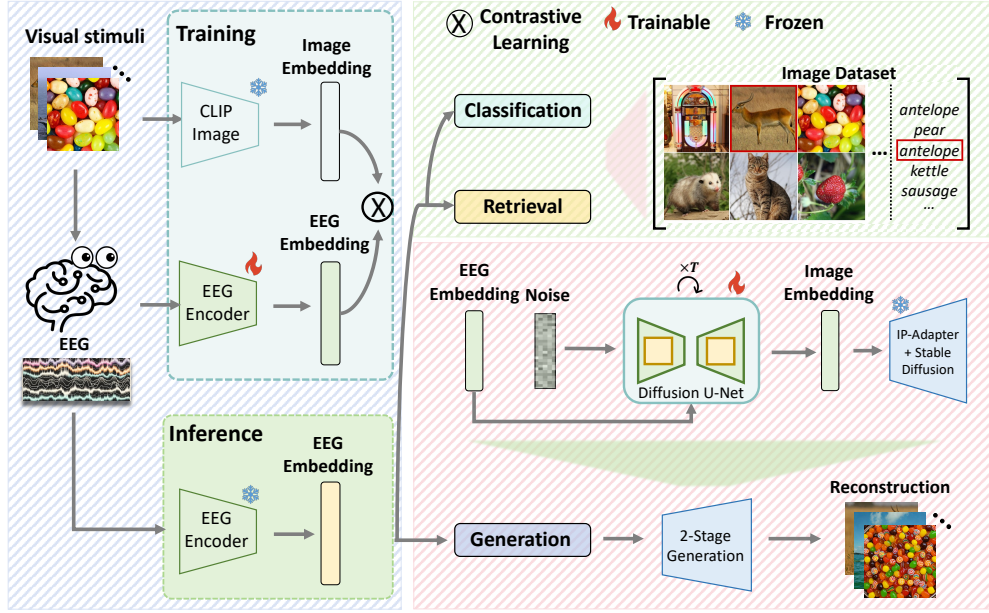


Fig. 2. EEG/MEG-based visual decoding and generation framework. The EEG encoder is designed as a flexible replacement component. After aligning with image features, the EEG features are used for zero-shot retrieval and classification tasks, and the reconstructed images are obtained through a two-stage generator.

gap in their performance compared to the fMRI-level performance. This gap is largely caused by weaknesses in its EEG encoder, which prevents EEG embeddings from effectively aligning with image embeddings.

To fill in the gap, we develop an EEG/MEG-based visual decoding framework, including a novel EEG encoder, called Adaptive Thinking Mapper (ATM), and a two-stage image generation strategy. We survey existing EEG encoder modules, such as EEGNetV4 [25], ShallowNet [37], and Conformer [44], and demonstrate through extensive comparative experiments and ablation studies that our method achieves state-of-the-art (SOTA) performance on image classification, retrieval, and generation tasks. Our work has three main contributions:

- We employ the attention module and a spatiotemporal convolution module in EEG encoder, which can be used in a plug-and-play manner, to extract representations in real-time for both EEG data and MEG data.
- Our brain encoder is trained with self-supervised contrastive learning framework, achieving SOTA performance on EEG and MEG datasets from natural image decoding tasks.
- We present a two-stage image generation strategy to facilitate the adjustment of the distribution from the original EEG data to the corresponding images. It employs a prior diffusion model that is conditioned on the EEG embeddings to generate the image embeddings, followed an enhanced Stable Diffusion module to generate images with EEG priors.

2 Method

To learn high-quality latent representations of EEG data, it is crucial to consider the spatial position of EEG channels and the spatiotemporal properties of EEG signals. Let T represent the

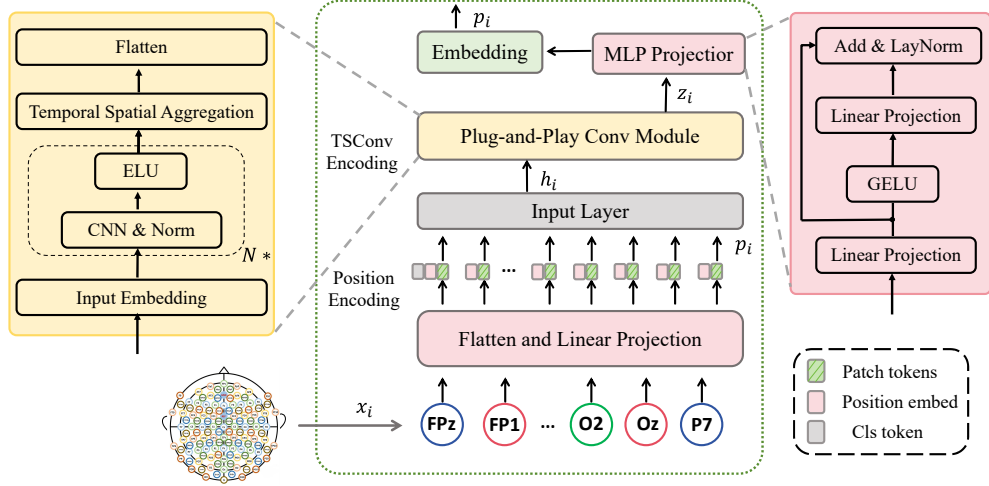


Fig. 3. The structure of EEG encoder ATM. According to the position of EEG channels and the spatiotemporal property of EEG signals, we design the *position encoding* and *temporospatial encoding* in ATM.

length of the time window of the data, C the number of EEG channels, and N the total number of data samples. Our objective is to derive EEG embeddings $Z_E = f(E) \in \mathbb{R}^{N \times F}$ from the brain activity data $E \in \mathbb{R}^{N \times C \times T}$, where f is the EEG encoder and F is the feature dimension of the embeddings. Concurrently, we use the CLIP model to extract image embeddings $Z_I \in \mathbb{R}^{N \times F}$ from images I . Our goal is to effectively align the EEG representation with the image representation, as illustrated in Fig. 2. In the training phase, the EEG encoder is trained with EEG and image pairs using a contrastive learning framework. In the inference phase, the EEG embeddings from the trained plug-and-play EEG encoder can be used for a variety of tasks, including EEG-based image classification, retrieval, and EEG-guided image generation.

2.1 ATM for EEG embedding

We develop an EEG encoder, called Adaptive Thinking Mapper (ATM), for aligning the original EEG signals to its feature representation space (Fig. 3). ATM is based on the Transformer Encoder and spatiotemporal convolution architecture. Specifically, we utilize a one-dimensional linear layer to project the input one-dimensional EEG data to the embedding dimension required by the Transformer model. These inputs are processed through a self-attention module to integrate the embeddings of input data and positional encoding. We first divide the input into fixed-size patches, with each image patch containing a fixed number of data points. Then, each patch is mapped to a high-dimensional embedding space through a linear layer. Subsequently, through the temporal aggregation process, we obtain the processed embedding representations. Notably, ATM addresses the inadequacies of other modules in modeling capabilities on the temporal scale through the Input Layer. For it has been reported that the spatiotemporal convolution module with a large convolution kernel is an effective way to represent EEG data with a small number of parameters [46], we use a similar spatiotemporal convolution (STConv)-based feature extraction module. The difference is our STConv Module is plug-and-play and can be flexibly replaced with different types of spatiotemporal convolution components as needed to adapt to various EEG/MEG datasets. Finally, MLP projection layer consists of M simple resid-

ual components and fully connected layers, with LayerNorm applied in the output to ensure the stability of training.

2.2 Image Embedding

Many previous studies have explored various training strategies to train deep neural networks for image embedding, such as VGG-19 and ResNet trained with supervised learning, CLIP trained with contrastive learning, and VAEs with self-supervised learning [49, 4, 46, 16]. They have reported that CLIP models pre-trained using the Vision Transformer (ViT) architecture perform better in a range of downstream tasks, including image decoding and reconstruction, compared to models trained using supervised learning methods (such as VGG, ResNet) and self-supervised VAE frameworks. Thus, in this study, we use CLIP for image embedding and align the CLIP’s output image representation, denoted as $Z_I \in \mathbb{R}^{N \times 1024}$, with the EEG embeddings. Before formal training, all images undergo standard preprocessing [34].

2.3 EEG guidance image generation

In this study, we present a two-stage pipeline for generating images that serve as visual stimuli for EEG recordings, as shown in the bottom right of Fig. 2. In the left of Fig. 3 we have obtained the EEG embeddings z_E for each image by the EEG encoder ATM. Now our goal is to use these EEG embeddings to generate the corresponding images. The joint distribution of images, EEG embeddings, and image embeddings can be expressed as $p(I, z_E, z_I) = p(z_I|z_E)p(I|z_I)$, corresponding to the prior diffusion and CLIP-guided generation, respectively. In **Stage I**, we first focus on the prior diffusion stage. Inspired by DALL-E 2 [35] and Mind’s Eyes [40], we train a diffusion model conditioned on the EEG embeddings \hat{Z}_E to learn the distribution of CLIP embeddings $p(z_I|z_E)$. In this stage, we construct a lightweight U-Net: $\epsilon_{\text{prior}}(z_I^t, t, z_E)$, where z_I^t represents the noisy CLIP embedding at diffusion time step t . We train the prior diffusion model using EEG and CLIP embeddings. Through this diffusion model, we can generate corresponding CLIP embeddings z_I from EEG embeddings as a prior for stage II. In **Stage II**, we employ the pre-trained SDXL [33] and IP-Adapter [59] models to model the generator $p(I|z_I)$, thereby sampling image I according to z_I . This stage mainly focuses on converting CLIP embeddings into corresponding images. Further details are provided in Appendix C.

2.4 Loss Function

Following the methodology outlined by Benchetrit et al. [4], we adopt a dual approach to loss functions, serving distinct objectives. For the classification and retrieval tasks, we only utilize the CLIP loss, which is inspired by the contrastive learning approach described in Radford et al. [34]. This loss function aids in aligning the EEG data E with corresponding image data I , thereby facilitating the identification of EEG-image pairs and maximizing the EEG classification boundaries. For the generation tasks, besides the CLIP loss, we add a Mean Squared Error (MSE) loss to facilitate learning in regression scenarios. Thus the overall loss function for our model is a combination of these two distinct loss types, expressed as:

$$\text{Loss} = \lambda \cdot L_{\text{CLIP}} + (1 - \lambda) \cdot L_{\text{MSE}}$$

Here, λ is a hyperparameter that balances the contribution of each loss type.

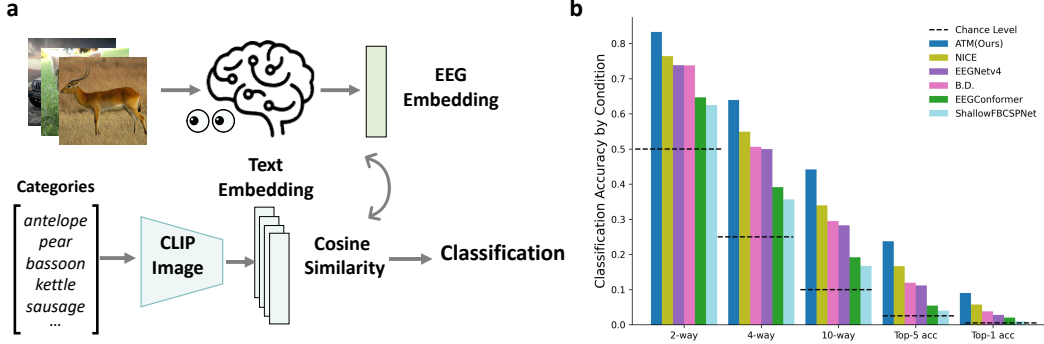


Fig. 4. EEG-based image classification. (a) The paradigm of EEG-based image classification. (b) Average accuracy across different methods in the subjects.

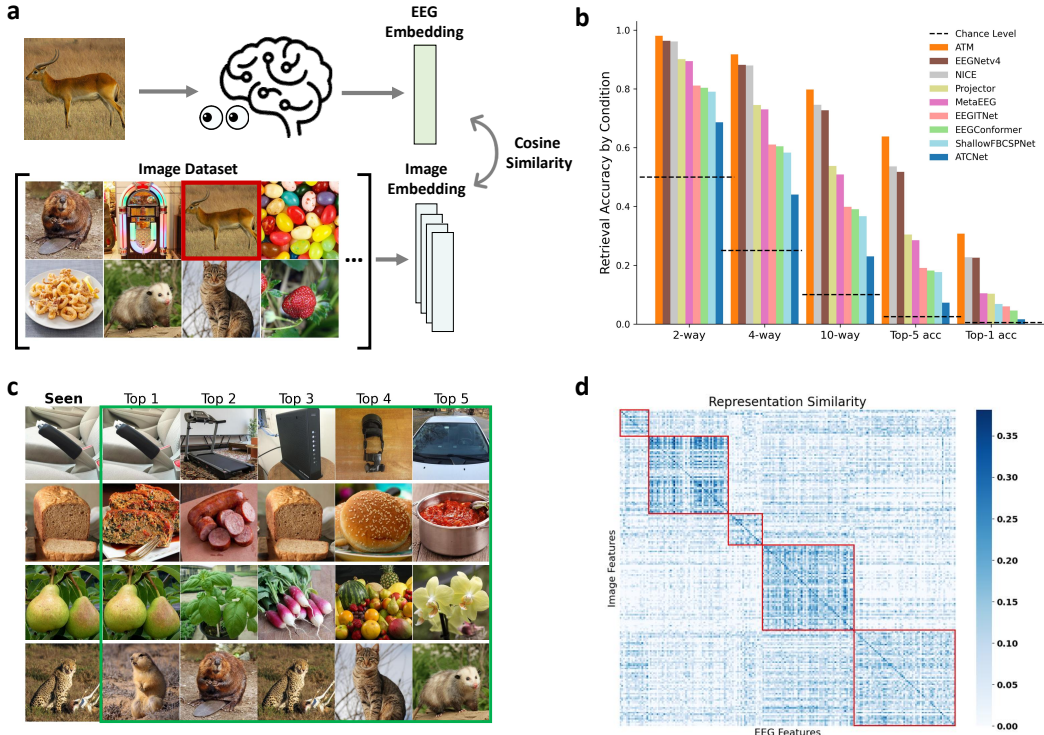


Fig. 5. EEG-based image retrieval. (a) The paradigm of EEG-based image retrieval. (b) Average accuracy across different methods in the subjects. (c) Images showing the top-5 accuracy in EEG-image retrieval tasks. See Appendix F for additional images results. (d) Representation similarity analysis. Clustering of image features and EEG features using a k-means algorithm with $k=5$ is performed, followed by the calculation of similarity between clusters. See Appendix E for additional Representational similarity results.

3 Experiments

3.1 Training and computational considerations

We conducted our experiments on the THINGS-EEG dataset’s training set [14, 16]. To verify the versatility of ATM for embedding electrophysiological data, we tested it on MEG data modality using the THINGS-MEG dataset [18]. We used the Adam optimizer [24] to train the across-subject model on a set of approximately 496,200 samples, and the within-subject model on a set of about 66,160 samples, with a learning rate of 3×10^{-4} and batch sizes of 16 and 1024. Our initial temperature parameter was set to 0.07. We tested on the zero-shot test dataset at the end of each training epoch during the training process. For fairness, all models’ hyperparameters were kept consistent. In our study, we compared the performance of different encoders on the within-subject test set and cross-subject (leave-one-subject-out) test set (see Appendix G).

3.2 EEG Decoding performance

The plug-and-play ATM can obtain the EEG embedding for the classification task using a simple cosine similarity measurement. We output the category with the highest cosine similarity (Fig. 4a). More details of the EEG-based image classification are in Appendix B. Fig. 4b presents the average accuracy across different methods in the subjects, and shows our method outperforms others.

Here, we test the effectiveness of ATM-extracted EEG embeddings in the image retrieval task. Fig. 5a shows the image retrieval process. We calculate the cosine similarity between the extracted EEG embeddings and the CLIP embeddings of the image dataset (with 200 images), and output the image with the highest similarity as the retrieved image. Fig. 5b shows the average results for all subjects in the in-subject test. We take the highest test accuracy in the training process as the statistical result. See the Appendix G for more detailed averages of test accuracy in subjects. Fig. 5c shows the Top-5 retrieved images corresponding to the real visual stimuli seen by subjects. Compared with the previous model, the Top-1 accuracy of our model is significantly improved, and the Top-5 images all maintain a high degree of similarity with the original images. We calculated the similarity of the EEG to the semantics and images. The similarity between the image and EEG is shown in Fig. 5d. We performed a representational similarity analysis, and we could observe different degrees of intra-class aggregation. This means that the EEG representation obtained is closer to the representation of the corresponding image itself than to the semantics.

Ablation study on ATM We systematically deconstructed and analyzed each layer of our EEG encoder module. We conducted an ablation study for each component in ATM (i.e., the MLP projector, the adaptive convolution module, the Input layer, and the spatial attention block). Notably, ATM is a flexible, plug-and-play module, which can be easily replaced with any form of convolutional component or even omitted. Appendix B.3 showed that the adaptive convolutional components significantly enhanced encoder performance, while the Input layer reduced the model’s training consumption and substantially improved the existing components’ capabilities. Surprisingly, our spatial attention module based on sine-cosine positional encoding improved encoder performance only when used alone, but the benefits were not as significant when combined with the Input layer.

3.3 Image Generation performance

Using the image generation task, we verify the effectiveness of ATM's EEG embedding and our two-stage generation model. Fig. 6a shows the process of generating images under the guidance of EEG embedding and evaluating the quality of the generated images. For one test image, we put EEG embedding of the subject viewing the image into the two-stage generator to guide the generation of the image. To evaluate the generation performance, we conducted an image retrieval task. Specifically, we extract the CLIP embedding of the generated images and calculate the similarity between the CLIP embeddings of all images in the image dataset to retrieve the generated image.

Fig. 6b shows the generation effect of the sample image. Fig. 6c shows the retrieval accuracy using generated images. The generated images have high semantic similarity with the seen images and have good diversity in low-level visual features, which can be manipulated by the guidance scale hyperparameter (Fig. 6d). Surprisingly, the retrieval accuracy using generated images is even higher than that using EEG embeddings, implying the benefit of our two-stage visual reconstruction for image retrieval (See Appendix C for Fig.11). We also report the decoding and reconstruction performance for EEG, MEG, and fMRI across various metrics in the Appendix D.

We visualize the best, medium and worst generated images in Fig. 7. We randomly selected the EEG data of a subject viewing 100 images, and extracted EEG embeddings to guide image generation. By calculating the cosine similarity of the CLIP embedding between the generated

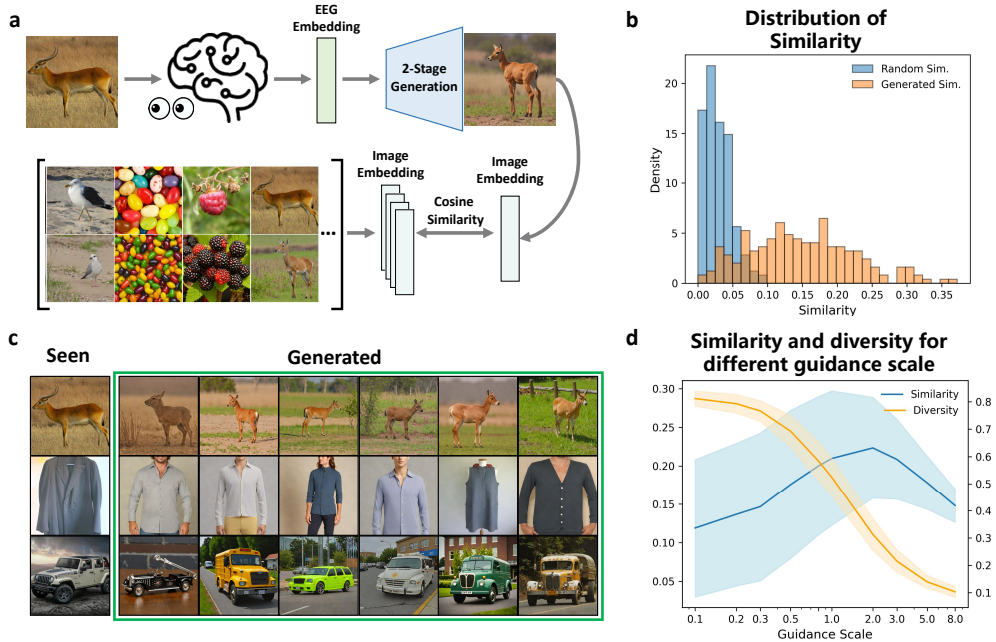


Fig. 6. EEG guidance image generation. (a) The paradigm of EEG guidance image generation. (b) The similarity between random visual objects and the EEG embeddings, and the similarity between generated visual objects and the target EEG embeddings. (c) Comparison between the original image and the image generated using the corresponding EEG data. (see Appendix C for details). (d) The similarity between visual objects and target EEG embeddings as the guidance scale changes, and the diversity of visual objects as the guidance scale changes. See Appendix F for additional results.

image and the original image, we found 12 images each with the best, medium and worst generation effects. It can be seen that in the best group, the generated image is not only highly consistent with the semantics of the original image, but also well retains the low-level visual features. in the medium group, the generated image maintains the semantic features of the original image, and the low-level visual features are well preserved. Visual features were altered. in the worst group, both semantic features and low-level visual features were altered.

3.4 Temporal analysis

To investigate the effects of EEG time window on visual decoding accuracy, we calculated the average top-1 classification accuracy for two different time windows: $[0, t]$, including the entire period from the onset of visual stimuli to time point t , and $[t-100, t]$, only including the data 100ms before time point t . We compared the accuracy with a randomly selected baseline (0.5% chance level) to test non-random predictive performance (Fig. 8). Our results show that within 500ms after visual stimulus presentation, the EEG signal decoding accuracy reaches an upper limit of about 30%, after which the accuracy no longer improves (Fig. 8a). The MEG decoding shows a similar profile as the time window expands (Fig. 8b). We exhibit the generated images under different EEG time windows, $[0, t]$ in Fig. 8c. The similarity between the generated images and the original images is low when the time window is less than 150ms, then this similarity gradually increase as the time window expands. After 500 milliseconds, EEG-guided image generation can reliably reveal the semantics of the images seen, such as aircraft carriers, modems, jelly beans, et al. Interestingly, we find differences in the optimal reconstruction time windows for different categories of images, for example, jelly beans (200ms) are faster than aircraft carrier (500ms), implying that the human brain may process different visual objects at different speeds. This finding highlights the advantage of EEG's high temporal resolution in studying fast visual processing compared with the lower temporal resolution of fMRI.

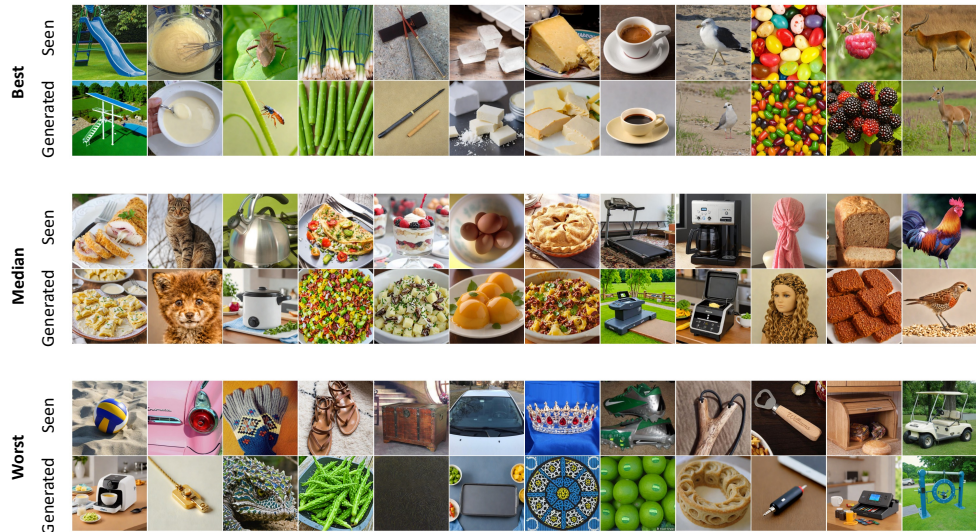


Fig. 7. Examples of EEG-guided visual reconstruction. From top to bottom, we exhibit the best, median, and worst 12 generated images, respectively. We show the images subjects seen and the generated images by our two-stage image generator. See Appendix F for additional results.

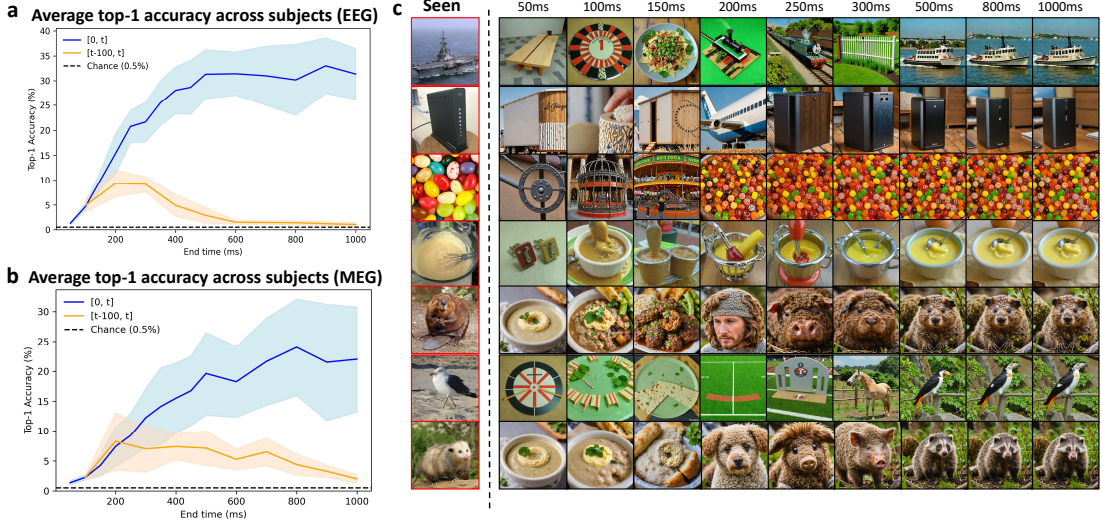


Fig. 8. Effects of different EEG/MEG time windows on EEG-guided visual retrieval and reconstruction. (a) The retrieval accuracy of the expanding EEG windows at intervals $[0, t]$ and at intervals $[t-100, t]$ respectively. (b) The retrieval accuracy of the expanding MEG windows. (c) Images reconstructed by EEG as the EEG window expands. When the EEG time window is greater than 200ms, the reconstructed image is reliable.

3.5 Spatial analysis

To examine the contribution of different brain regions to visual decoding, we divided the EEG electrodes from the THING-EEG data into five distinct brain regions (i.e., Frontal, Temporal, Center, Parietal, Occipital regions in Fig. 9a), and then conducted ablation experiments on retrieval task (Fig. 9b) and the reconstruction task (Fig. 9c). The results showed that using information from all brain regions is optimal, for both retrieval and generation tasks. The occipital had the highest retrieval accuracy and reconstruction performance compared to other regions. Parietal and temporal regions contain some semantic information, whereas frontal and central regions contribute the least useful information to the visual decoding.

4 Related works

Visual decoding using neural signal: Decoding visual information from our brain has been a long-standing pursuit in neuroscience and computer science [30, 20]. Some progress has been made in decoding steady-state visual stimuli. However, accurately and rapidly decoding semantic information in natural images remains a challenge [42]. fMRI has been widely used to estimate semantic and shape information in visual processing within the brain [48, 19]. However, the demand for high-speed and practical applications in brain-computer interfaces calls for alternative approaches. EEG, due to its high temporal resolution and portability, emerges as a promising option [53]. Yet, the overall performance across different subjects and biological plausibility remains unresolved [1]. Furthermore, previous approaches often relied on supervised learning methods with limited image categories, overlooking the intrinsic relationship between image stimuli and brain responses [28, 41, 27].

Neural decoding for EEG signal: Previous studies have shown the efficacy of spatiotemporal modules in representing neural data [37, 25]. For example, lightweight convolutional neu-

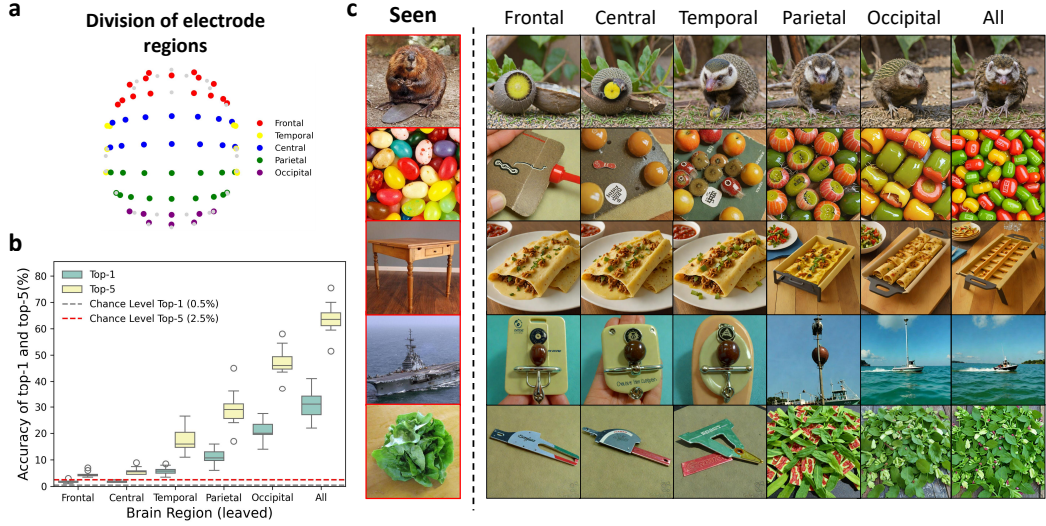


Fig. 9. EEG-guided visual retrieval and reconstruction using EEG signals from different brain regions. (a) The EEG electrodes assigned to five brain regions. (b) Top-1 and top-5 retrieval accuracy, using only the EEG channels in each leaved region and all channels. (c) Reconstructed images obtained using only the electrode channels in each individual region and all channels.

ral networks such as EEGNet and ShallowNet [37] have achieved considerable performance in small EEG and MEG datasets. Using contrastive learning, it has been shown that merely using convolutional neural networks and projection layers can yield satisfactory results on neural datasets [6]. More recently, Benchetrit et al proposed a B.D. encoder for MEG embedding, allowing real-time MEG-based reconstruction of visual perception [4]. Song et al. presented an EEG encoder using ShallowNet spatiotemporal convolution module with a large convolution kernel with a few parameters for EEG embedding, resulting in favorable performance on EEG-based visual decoding [46].

Limitations of previous studies: Previous EEG studies are primarily oriented toward understanding visual perception in the human brain rather than maximizing EEG decoding performance. Thus the visual decoding performance is far from optimal. Specifically, previous studies have trained linear models to (1) classify a small set of images from brain activity [15, 23], (2) to predict brain activity from the latent representations of images [8], or (3) to quantify the similarity analysis between these two patterns with representational similarity [8, 15, 14, 3]. While these studies also utilize image embeddings, their linear decoders are limited to classifying a small group of object categories or distinguishing image pairs. Moreover, several deep neural networks have been applied to maximize classification of speech [10], cognitive load [21], and images [32, 29, 2] in EEG recordings. [32] proposed a deep convolutional neural network for classifying natural images using EEG signals. Unfortunately, the experiment presented all images of the same category in a single block, probably misleading the decoder to rely on autocorrelated noise rather than the hidden informative patterns of brain activity [27]. Also, these EEG studies only classify a relatively small number of image categories.

5 Discussion and Conclusion

In this study, we developed an EEG-based image decoding and reconstruction framework. Employing self-supervised learning, our method enables the model to achieve better generalization performance in different tasks. To our knowledge, this is the first instance of EEG decoding achieving end-to-end image reconstruction with fMRI-level performance.

Technical Impact: Our technical contributions are mainly on the EEG encoder and the two-stage image generator (Fig. 2). First, we developed the ATM, a plug-and-play EEG encoder which can efficiently extract EEG/MEG features for the three visual decoding tasks. Our comprehensive experiments of the EEG encoder (Fig. 3), compared to various architectures and training methods, achieves SOTA performance across various metrics and tasks (Figs. 1b, 4, 5). Second, the two-stage EEG guidance image generation achieves performance close to fMRI using only EEG data (Figs. 6, 7, Tab. 3, 4), and this method is compatible with MEG data (Figs. 1c, 8b). By comparing EEG embeddings and image embeddings obtained through prior diffusion, we demonstrated that EEG embeddings obtained via contrastive learning alone were insufficient for generating credible images (Appendix C), suggesting that our two-stage generation strategy could effectively enhance generation performance even with limited data.

Neuroscience Insights: Our results offer insights into the relationship between brain activity and visual perception. We analyzed EEG-based visual decoding within different time windows to examine when visual information is perceived in the brain (Fig. 8). Our results revealed that visual information in EEG data is predominantly contained within the 200-400ms range (Fig. 8a), consistent with previous EEG studies [49, 16, 46]. Interestingly, the visual information in MEG data last up to 800ms, much longer than EEG (Fig. 8b), in line with the results reported by a previous MEG study [4, 46]. We also found that EEG performs better than MEG in visual tasks (See Appendix D for Tab. 4), which is different from other fields, such as speech decoding [10]. In addition, through ablation experiments of spatial information, we found that visual information is mainly encoded in the occipital and parietal areas (Fig. 9). Using the image reconstruction tasks, we can visualize the information encoded in the brain, providing a window for vision researchers to explore how humans perceive visual information.

Interesting Phenomena and Future Directions: Our study uncovered intriguing phenomena, shedding lights on the future direction of EEG decoding. First, there are non-negligible performance differences between cross-subject and within-subject settings. This performance gap arises from inter-subject differences in EEG signals [13, 58], likely attribute to heterogeneity in individual brain, differences in visual perception between individuals, and even shifts in noise distribution during EEG recording. To address this cross-subject challenge, it calls for more efforts on EEG encoder, such as more flexible neural network architectures or training with larger EEG dataset. Transfer learning and meta-learning are also future directions worth exploring [55, 54, 57]. On the other hand, large EEG models pre-trained on massive EEG datasets may be the ultimate solution for visual decoding tasks [9, 7]. Nevertheless, how to unify various electrode montages of different EEG datasets when pre-training large EEG models is a challenge. EEG source localization, which converts senior-level EEG signals into the standard brain source space [52, 50], might be a potential solution. Moreover, our EEG-based image reconstruction results are somewhat limited by the visual features used from CLIP. For instance, it is easy to reconstruct semantics but difficult to preserve low-level visual feature aspects. This limitation leads to generated images lacking detail and richness. Future studies could use multiple different visual features to align EEG and image data. This proposition finds support in similar methodologies applied in fMRI-based studies [40, 26], which combine high-level semantic features extracted by CLIP with low-level visual features from VAE to improve consistency.

Acknowledgements

This work is supported by the National Key R&D Program of China (2021YFF1200804), Shenzhen Science and Technology Innovation Committee (20200925155957004, KCXFZ20201221173400001, SGDX2020110309280100).

This work originated as a course project in the BI&AI 2023 course at SUSTech, and the author would like to thank course project members, Yuanhao Fan and Zihong Wu, for their contributions to the early stages of this work. Thank Haoyang Qin for his time and advice.

References

- [1] Ahmed, H., Wilbur, R.B., Bharadwaj, H.M., Siskind, J.M.: Object classification from randomized eeg trials pp. 3845–3854 (2021) [10](#)
- [2] Bagchi, S., Bathula, D.R.: Eeg-convtransformer for single-trial eeg-based visual stimulus classification. *Pattern Recognition* **129**, 108757 (2022) [11](#)
- [3] Bankson, B.B., Hebart, M.N., Groen, I.I., Baker, C.I.: The temporal evolution of conceptual object representations revealed through models of behavior, semantics and deep neural networks. *NeuroImage* **178**, 172–182 (2018) [11](#)
- [4] Benchettit Y, Banville H, K.J.R.: Brain decoding: toward real-time reconstruction of visual perception. *arXiv* **2310**, 19812 (2023) [5](#), [11](#), [12](#), [17](#), [18](#), [22](#)
- [5] Caron, M., Misra, I., Mairal, J., et al.: Unsupervised learning of visual features by contrasting cluster assignments. *Advances in neural information processing systems* **33**, 9912–9924 (2020) [21](#)
- [6] Chen, T., Kornblith, S., Norouzi, M., et al.: A simple framework for contrastive learning of visual representations. In: *International conference on machine learning*. pp. 1597–1607. PMLR (2020) [11](#)
- [7] Chen, X., Teng, X., Chen, H., Pan, Y., Geyer, P.: Toward reliable signals decoding for electroencephalogram: A benchmark study to eegnex. *Biomedical Signal Processing and Control* **87**, 105475 (2024) [12](#)
- [8] Cichy, R.M., Pantazis, D.: Multivariate pattern analysis of meg and eeg: A comparison of representational structure in time and space. *NeuroImage* **158**, 441–454 (2017) [2](#), [11](#)
- [9] Cui, W., Jeong, W., Thölke, P., Medani, T., Jerbi, K., Joshi, A.A., Leahy, R.M.: Neuro-gpt: Developing a foundation model for eeg. *arXiv preprint arXiv:2311.03764* (2023) [12](#)
- [10] Défossez, A., Caucheteux, C., Rapin, J., Kabeli, O., King, J.R.: Decoding speech perception from non-invasive brain recordings. *Nature Machine Intelligence* **5**(10), 1097–1107 (2023) [11](#), [12](#)
- [11] Du, C., Fu, K., Li, J., He, H.: Decoding visual neural representations by multimodal learning of brain-visual-linguistic features. *IEEE Transactions on Pattern Analysis and Machine Intelligence* (2023) [22](#)
- [12] Fang, T., Zheng, Q., Pan, G.: Alleviating the semantic gap for generalized fmri-to-image reconstruction. In: *Thirty-seventh Conference on Neural Information Processing Systems* (2023) [2](#)
- [13] Gibson, E., Lobaugh, N.J., Joordens, S., McIntosh, A.R.: Eeg variability: Task-driven or subject-driven signal of interest? *NeuroImage* **252**, 119034 (2022) [12](#)
- [14] Gifford, A.T., Dwivedi, K., Roig, G., Cichy, R.M.: A large and rich eeg dataset for modeling human visual object recognition. *NeuroImage* **264**, 119754 (2022) [2](#), [7](#), [11](#), [16](#)
- [15] Grootswagers, T., Robinson, A.K., Carlson, T.A.: The representational dynamics of visual objects in rapid serial visual processing streams. *NeuroImage* **188**, 668–679 (2019) [11](#)

- [16] Grootswagers, T., Zhou, I., Robinson, A.K., Hebart, M.N., Carlson, T.A.: Human eeg recordings for 1,854 concepts presented in rapid serial visual presentation streams. *Scientific Data* **9**(1), 3 (2022) [2](#), [5](#), [7](#), [12](#), [16](#)
- [17] Guggenmos, M., Sterzer, P., Cichy, R.M.: Multivariate pattern analysis for meg: A comparison of dissimilarity measures. *Neuroimage* **173**, 434–447 (2018) [16](#)
- [18] Hebart, M.N., Contier, O., Teichmann, L., Rockter, A.H., Zheng, C.Y., Kidder, A., Corriveau, A., Vaziri-Pashkam, M., Baker, C.I.: Things-data, a multimodal collection of large-scale datasets for investigating object representations in human brain and behavior. *Elife* **12**, e82580 (2023) [7](#), [16](#)
- [19] Ho, J.K., Horikawa, T., Majima, K., Cheng, F., Kamitani, Y.: Inter-individual deep image reconstruction via hierarchical neural code conversion. *NeuroImage* **271**, 120007 (2023) [10](#)
- [20] Jia, C., Yang, Y., Xia, Y., Chen, Y.T., Parekh, Z., Pham, H., Le, Q., Sung, Y.H., Li, Z., Duerig, T.: Scaling up visual and vision-language representation learning with noisy text supervision. In: International conference on machine learning. pp. 4904–4916. PMLR (2021) [10](#)
- [21] Jiao, Z., Gao, X., Wang, Y., Li, J., Xu, H.: Deep convolutional neural networks for mental load classification based on eeg data. *Pattern Recognition* **76**, 582–595 (2018) [11](#)
- [22] Karras, T., Aittala, M., Aila, T., Laine, S.: Elucidating the design space of diffusion-based generative models. *Advances in Neural Information Processing Systems* **35**, 26565–26577 (2022) [19](#)
- [23] King, J.R., Wyart, V.: The human brain encodes a chronicle of visual events at each instant of time through the multiplexing of traveling waves. *Journal of Neuroscience* **41**(34), 7224–7233 (2021) [11](#)
- [24] Kingma, D.P., Ba, J.: Adam: A method for stochastic optimization. arXiv preprint arXiv:1412.6980 (2014) [7](#)
- [25] Lawhern, V.J., Solon, A.J., Waytowich, N.R., et al.: Eegnet: a compact convolutional neural network for eeg-based brain–computer interfaces. *Journal of Neural Engineering* **15**(5), 056013 (2018) [3](#), [10](#)
- [26] Li, H., Wu, H., Chen, B.: Neuraldiffuser: Controllable fmri reconstruction with primary visual feature guided diffusion. arXiv preprint arXiv:2402.13809 (2024) [12](#)
- [27] Li, R., Johansen, J.S., Ahmed, H., Ilyevsky, T.V., Wilbur, R.B., Bharadwaj, H.M., Siskind, J.M.: The perils and pitfalls of block design for eeg classification experiments. *IEEE Transactions on Pattern Analysis and Machine Intelligence* **43**(1), 316–333 (2020) [10](#), [11](#)
- [28] Liu, Y., Ma, Y., Zhou, W., Zhu, G., Zheng, N.: Brainclip: Bridging brain and visual-linguistic representation via clip for generic natural visual stimulus decoding from fmri. arXiv preprint arXiv:2302.12971 (2023) [2](#), [10](#)
- [29] McCartney, B., Devereux, B., Martinez-del Rincon, J.: A zero-shot deep metric learning approach to brain–computer interfaces for image retrieval. *Knowledge-Based Systems* **246**, 108556 (2022) [11](#)
- [30] Miyawaki, Y., Uchida, H., Yamashita, O., Sato, M.a., Morito, Y., Tanabe, H.C., Sadato, N., Kamitani, Y.: Visual image reconstruction from human brain activity using a combination of multiscale local image decoders. *Neuron* **60**(5), 915–929 (2008) [10](#)
- [31] Ozcelik, F., VanRullen, R.: Natural scene reconstruction from fmri signals using generative latent diffusion. *Scientific Reports* **13**(1), 15666 (2023) [22](#)
- [32] Palazzo, S., Spampinato, C., Kavasidis, I., Giordano, D., Schmidt, J., Shah, M.: Decoding brain representations by multimodal learning of neural activity and visual features. *IEEE Transactions on Pattern Analysis and Machine Intelligence* **43**(11), 3833–3849 (2020) [11](#)
- [33] Podell, D., English, Z., Lacey, K., Blattmann, A., Dockhorn, T., Müller, J., Penna, J., Rombach, R.: Sdxl: Improving latent diffusion models for high-resolution image synthesis. arXiv preprint arXiv:2307.01952 (2023) [5](#), [21](#)

- [34] Radford, A., Kim, J.W., Hallacy, C., Ramesh, A., Goh, G., Agarwal, S., Sastry, G., Askell, A., Mishkin, P., Clark, J., et al.: Learning transferable visual models from natural language supervision. In: International conference on machine learning. pp. 8748–8763. PMLR (2021) 5
- [35] Ramesh, A., Dhariwal, P., Nichol, A., Chu, C., Chen, M.: Hierarchical text-conditional image generation with clip latents. arXiv preprint arXiv:2204.06125 **1**(2), 3 (2022) 5
- [36] Sauer, A., Lorenz, D., Blattmann, A., Rombach, R.: Adversarial diffusion distillation. arXiv preprint arXiv:2311.17042 (2023) 21
- [37] Schirrmeister, R.T., Springenberg, J.T., Fiederer, L.D.J., Glasstetter, M., Eggensperger, K., Tangermann, M., Hutter, F., Burgard, W., Ball, T.: Deep learning with convolutional neural networks for eeg decoding and visualization. *Human Brain Mapping* **38**(11), 5391–5420 (2017) 2, 3, 10, 11
- [38] Schonfeld, E., Ebrahimi, S., Sinha, S., et al.: Generalized zero-and few-shot learning via aligned variational autoencoders. In: Proceedings of the IEEE/CVF Conference on Computer Vision and Pattern Recognition. pp. 8247–8255 (2019) 22
- [39] Scotti, P., Banerjee, A., Goode, J., et al.: Reconstructing the mind’s eye: fmri-to-image with contrastive learning and diffusion priors. *Advances in Neural Information Processing Systems* **36** (2024) 22
- [40] Scotti, P.S., Banerjee, A., Goode, J., Shabalin, S., Nguyen, A., Cohen, E., Dempster, A.J., Verlinde, N., Yundler, E., Weisberg, D., et al.: Reconstructing the mind’s eye: fmri-to-image with contrastive learning and diffusion priors. arXiv preprint arXiv:2305.18274 (2023) 2, 5, 12
- [41] Shen, G., Dwivedi, K., Majima, K., Horikawa, T., Kamitani, Y.: End-to-end deep image reconstruction from human brain activity. *Frontiers in computational neuroscience* **13**, 21 (2019) 10
- [42] Shi, N., Li, X., Liu, B., Yang, C., Wang, Y., Gao, X.: Representative-based cold start for adaptive ssvep-bci. *IEEE Transactions on Neural Systems and Rehabilitation Engineering* **31**, 1521–1531 (2023) 10
- [43] Shi, Y., Paige, B., Torr, P.: Variational mixture-of-experts autoencoders for multi-modal deep generative models. *Advances in neural information processing systems* **32** (2019) 22
- [44] Song, Y., Zheng, Q., Liu, B., et al.: Eeg conformer: Convolutional transformer for eeg decoding and visualization. *IEEE Transactions on Neural Systems and Rehabilitation Engineering* **31**, 710–719 (2022) 3
- [45] Song, Y., Sohl-Dickstein, J., Kingma, D.P., Kumar, A., Ermon, S., Poole, B.: Score-based generative modeling through stochastic differential equations. In: International Conference on Learning Representations (2020) 19
- [46] Song, Y., Liu, B., Li, X., Shi, N., Wang, Y., Gao, X.: Decoding natural images from eeg for object recognition. arXiv preprint arXiv:2308.13234 (2023) 2, 4, 5, 11, 12, 17, 18
- [47] Sutter, T.M., Daunhawer, I., Vogt, J.E.: Generalized multimodal elbo. In: International Conference on Learning Representations (2020) 22
- [48] Takagi, Y., Nishimoto, S.: High-resolution image reconstruction with latent diffusion models from human brain activity. In: Proceedings of the IEEE/CVF Conference on Computer Vision and Pattern Recognition. pp. 14453–14463 (2023) 10
- [49] Teichmann, L., Hebart, M.N., Baker, C.I.: Multidimensional object properties are dynamically represented in the human brain. *bioRxiv* (2023) 5, 12
- [50] Wang, S., Wei, C., Lou, K., Gu, D., Liu, Q.: Advancing eeg/meg source imaging with geometric-informed basis functions. arXiv preprint arXiv:2401.17939 (2024) 12
- [51] Wang, Z., Bovik, A.C., Sheikh, H.R., et al.: Image quality assessment: from error visibility to structural similarity. *IEEE transactions on image processing* **13**(4), 600–612 (2004) 21

- [52] Wei, C., Lou, K., Wang, Z., et al.: Edge sparse basis network: A deep learning framework for eeg source localization. In: 2021 International Joint Conference on Neural Networks (IJCNN). pp. 1–8. IEEE (2021) [12](#)
- [53] Willett, F.R., Avansino, D.T., Hochberg, L.R., Henderson, J.M., Shenoy, K.V.: High-performance brain-to-text communication via handwriting. *Nature* **593**(7858), 249–254 (2021) [10](#)
- [54] Wu, D., Jiang, X., Peng, R.: Transfer learning for motor imagery based brain–computer interfaces: A tutorial. *Neural Networks* **153**, 235–253 (2022) [12](#)
- [55] Wu, D., Xu, Y., Lu, B.L.: Transfer learning for eeg-based brain–computer interfaces: A review of progress made since 2016. *IEEE Transactions on Cognitive and Developmental Systems* **14**(1), 4–19 (2020) [12](#)
- [56] Wu, M., Goodman, N.: Multimodal generative models for scalable weakly-supervised learning. *Advances in neural information processing systems* **31** (2018) [22](#)
- [57] Xie, Y., Wang, K., Meng, J., Yue, J., Meng, L., Yi, W., Jung, T.P., Xu, M., Ming, D.: Cross-dataset transfer learning for motor imagery signal classification via multi-task learning and pre-training. *Journal of Neural Engineering* **20**(5), 056037 (2023) [12](#)
- [58] Xu, L., Xu, M., Ke, Y., An, X., Liu, S., Ming, D.: Cross-dataset variability problem in eeg decoding with deep learning. *Frontiers in human neuroscience* **14**, 103 (2020) [12](#)
- [59] Ye, H., Zhang, J., Liu, S., Han, X., Yang, W.: Ip-adapter: Text compatible image prompt adapter for text-to-image diffusion models. *arXiv preprint arXiv:2308.06721* (2023) [5, 21](#)

A Datasets for experiments

A.1 EEG dataset

We conducted our experiments on the THINGS-EEG dataset’s training set [14, 16]. This dataset includes a large EEG corpus from 10 human subjects during the visual task. The experiment employed the Rapid Serial Visual Presentation (RSVP) paradigm for orthogonal target detection tasks to ensure that participants attended to the visual stimuli. All 10 participants completed 4 equivalent experiments, resulting in 10 datasets with 16,540 training image conditions repeated 4 times, and 200 testing image conditions repeated 80 times, totaling $(16,540 \text{ training image conditions} \times 4 \text{ repetitions}) + (200 \text{ testing image conditions} \times 80 \text{ repetitions}) = 82,160$ image trials. Original data were collected using a 64-channel system at a sampling rate of 1000 Hz. After signal denoising, epoch data were downsampled to 100 Hz, selecting 17 channels covering the occipital and parietal cortex. Instead of using the raw dataset, we chose to filter it to $[0.1, 100]$ Hz, retaining 63 channels of the original EEG data at a sampling rate of 1000 Hz. For preprocessing, we segmented the EEG data from 0 to 1000 ms after the stimulus onset into trials. Baseline correction was performed using the mean of the 200 ms pre-stimulus data. All electrodes were retained and downsampled to 250 Hz for analysis, and multivariate noise normalization was applied to the training data [17]. To improve signal-to-noise ratio, we averaged across the four EEG trials from the same image in the test set, while keeping each EEG trial in the training setting. We compared the effects of averaging across EEG trials and found it indeed improved the performance.

A.2 MEG dataset

To verify the versatility of ATM for embedding electrophysiological data, we tested it on MEG data modality using the THINGS-MEG dataset [18]. It includes 271-channel MEG data from

4 subjects with 12 MEG sessions. The training dataset has $1854 \text{ Concepts} \times 12 \text{ images} \times 1$ repetition, and the test dataset has $\text{concepts} \times 1 \text{ image} \times 12 \text{ repetitions}$ for 200 times. Here, we discarded 200 testing concepts from the training set to construct the same zero-shot task as with the THINGS-EEG. Each image in the THINGS-MEG was displayed for 500 ms. There was a fixed time for each image of 1000 ± 200 ms. Continuous MEG data from -100 ms to 1300 ms was segmented into trials after the stimulus onset from 0 to 1000 ms. Preprocessing was performed using a bandpass filter of [0.1, 40] Hz and baseline correction after downsampling to 200 Hz. Note that due to the small number of participants, no statistical analysis was performed on the MEG dataset. We compared our approach with advanced methods i.e. NICE [46] and B.D. [4] for classification and retrieval tasks on the MEG dataset. Similar to [46], we directly used the stimulus images to match the template, rather than other images belonging to the concept.

B More Implementation Details

B.1 Evaluation metric implementation

Classification accuracy As CLIP has been designed to align text and image modalities, we also leverage its text encoder for EEG classification using the text embeddings of categories. This approach utilizes CLIP’s text encoding capabilities to facilitate EEG classification. We conducted zero-shot classification tests on the THINGS-EEG dataset. We employed **Top-K accuracy** as a metric for performance evaluation. Specifically, we assessed performance based on the Top-k (where $k=1, 5$) predictions. This means a classification is considered correct if the true category is among the model’s Top-k predicted categories. We conducted tests for both within-subject and leave-one-subject-out classification accuracy, enabling a comprehensive evaluation of the model’s performance across different scenarios. Additionally, for each test instance, we extracted embeddings of $N-1$ unrelated samples from the test set as inputs. This means, apart from the entire test set, the model evaluated by **N-Way accuracy** (where $N=2, 4, 10$ in our experiments) on the test set. We report these results in Appendix G.

Retrieval accuracy Similar to the classification task, in the retrieval task, the objective is to retrieve the Top-K images most related to a given stimulus image via its corresponding EEG signal. This implies that by merely changing the text embeddings of image labels used during prediction, to image embeddings, we can transition the task from classification to image retrieval. The performance in retrieval tasks is superior to classification tasks as using image embeddings in training. We conducted a detailed comparison of different methods in terms of their Top-K retrieval accuracy in image retrieval tasks. Given that contrastive learning is known to be sensitive to batch size, we also compared the performance improvement of different methods under varying batch sizes (batch size=16, 1024) (Appendix G).

Generation accuracy The generation task presents more challenges than the other tasks. In this phase, EEG representations are fed into a two-stage generator. For each image condition in the test set, we generate 1 images from 10 subjects based on the corresponding EEG signal. Subsequently, image retrieval is performed for each generated image. The Top-1 and Top-5 accuracies are calculated. Since we utilized CLIP for alignment and did not extract lower-level visual features from the EEG, this metric is particularly useful. It helps in evaluating the semantic alignment between the generated images and their original counterparts.

B.2 Computing methods implementation

In the upstream EEG encoder part, we compared various methods. For the B.D. method [4], we replicated the network structure as described in the original work, with the difference being in the shape of the input data, due to the original study’s focus on MEG. It is worth mentioning that we used the retention test method in the testing process, so the strategy of joint subject training is not suitable for our task. We modify its subject-wise layer as an Input layer for modeling the time dimension. Regarding the [46], we also reproduced the EEG encoder as described in their paper, using spatiotemporal convolution modules and EEG projection modules with the same convolution parameters. To ensure fairness, we did not use the same hyperparameters as in the original paper. Instead, we chose settings that yielded excellent results upon reproduction. Across all methods, we used identical hyperparameters, apart from the network structures. These included batch size, optimizer, initial learning rate, and temperature parameters.

B.3 Architecture details

Table 1. Brain module configuration for use with a target latent of size 1024

Layer	Input shape	Output shape	# parameters
Spatial attention block	(N, C, T)	(N, C, T)	553,078
Input layer	(N, C, T)	(N, C, T)	62,750
Plug-and-Play Conv module	(N, C, T)	$(N, H1, H2)$	103,680
Temporal aggregation	$(N, H1, H2)$	$(N, H1*H2)$	0
MLP projector	$(N, H1*H2)$	$(N, 1024)$	2,527,232
Total			3,246,741

B.4 Training details

In the initial design of the EEG encoder module, we adopted two approaches to guide model predictions: text embedding and image embedding. Due to the differences in feature granularity, alignments favoring image embedding tend to perform better in image retrieval and classification tasks. During the training process using contrastive learning, we found that a batch size of 16 is a prudent choice across all models. A batch size of 1024 means that a sufficient number of samples are compared in a single training step, which requires the model to have a higher noise

Table 2. Ablation study on the ATM model’s different components for THINGS-EEG retrieval.

Module	MLP	AdaConv	IL	SA	TOP-1	TOP-5
ATM-S	✓				8.01 ±1.97	25.41±5.74
	✓	✓			21.55±6.26	50.78±8.77
	✓	✓	✗	✓	23.57±6.00	53.50±7.26
	✓	✓	✓	✗	27.71±6.22	58.71±7.49
	✓	✓	✓	✓	26.49±5.81	56.58±8.67
ATM-E	✓				8.01 ±1.97	25.41±5.74
	✓	✓			18.67±5.48	46.31±9.11
	✓	✓	✗	✓	21.11±5.56	50.48±7.74
	✓	✓	✓	✗	24.64±5.97	54.17±5.93
	✓	✓	✓	✓	22.43±5.41	51.24±7.27

resistance capability. As observed in Tab. 5 and Tab. 6, larger batch sizes have the potential to achieve better performance and definite training efficiency gains across most methods. To improve the signal-to-noise ratio of EEG, we averaged 80 repeated data in the test set, a method similar to seeking Event-Related Potentials (ERP). To make full use of the training data volume, we did not average the 4 repetitions in the training set but instead fed all EEG data into the model for learning.

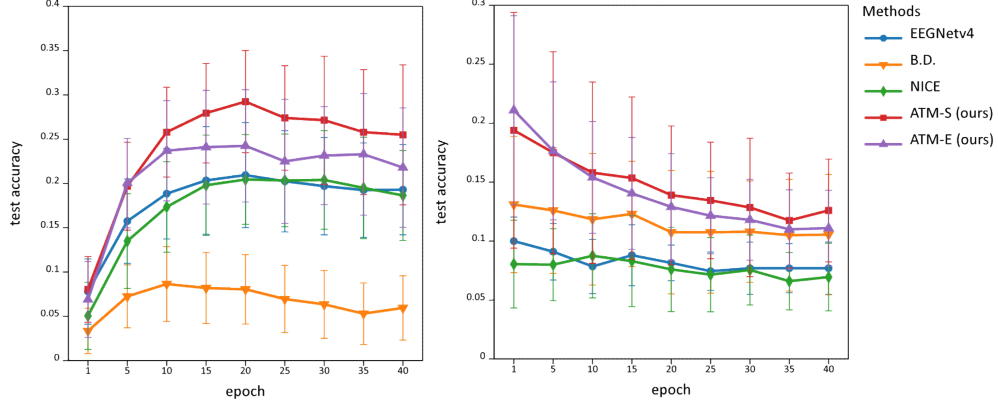


Fig. 10. Test accuracy during training. (a) Training of within-subject model. (b) Training of across-subject model. We compared 5 different EEG encoding models, including EEGNetv4, B.D., NICE, ATM-S and ATM-E.

C Details of EEG guidance image generation

Here, we provide a concise overview of the conditional diffusion model framework used in EEG-guided image generation, following the presentation of continuous-time diffusion models in [45, 22].

Diffusion models Diffusion Models (DMs) engage in a generative process by transforming high-variance Gaussian noise into structured data representations. This transformation is achieved by gradually reducing noise levels across a sequence of steps. Specifically, we begin with a high-variance Gaussian noise $x_M \sim \mathcal{N}(0, \sigma_{\max}^2)$ and systematically denoise it through a series of steps to obtain $x_t \sim p(x_t; t)$, where $\sigma_t < \sigma_{t+1}$ and $\sigma_M = \sigma_{\max}$. For a well-calibrated DM, and with $\sigma_0 = 0$, the final x_0 aligns with the original data distribution.

Sampling process The sampling in DMs is implemented by numerically simulating a Probability Flow ordinary differential equation (ODE) or a stochastic differential equation (SDE). The ODE is represented as:

$$dx = -\dot{\sigma}(t)\sigma(t)\nabla_x \log p(x; t)dt, \quad (1)$$

where $\nabla_x \log p(x; t)$ is the score function, and $\sigma(t)$ is a pre-defined schedule with its time derivative $\dot{\sigma}(t)$. The SDE variant includes a Langevin diffusion component and is expressed as:

$$\begin{aligned}
dx = & -\dot{\sigma}(t)\sigma(t)\nabla_x \log p(x; t)dt \\
& -\beta(t)\sigma^2(t)\nabla_x \log p(x; t)dt \\
& +\sqrt{2\beta(t)}\sigma(t)d\omega_t,
\end{aligned} \tag{2}$$

where $d\omega_t$ is the standard Wiener process.

Training of DMs The core of DM training is to learn a model $s_\theta(x; t)$ for the score function. This is typically achieved through denoising score matching (DSM), where ϵ_θ is a learnable denoiser. The training process can be formulated as:

$$\mathbb{E}_{(x_0, c) \sim p_{\text{data}}(x_0, c), (n_t, t) \sim p(n_t, t)} [\|\epsilon_\theta(x_0 + n_t; t, c) - x_0\|_2^2], \tag{3}$$

where n_t is Gaussian noise with variance σ_t^2 , and c represents a condition.

C.1 Stage I - EEG-Conditioned Diffusion

The initiation of the EEG-conditioned diffusion phase is paramount in our EEG-based image generation framework, leveraging the classifier-free guidance strategy alongside data pairs of CLIP embeddings and EEG embeddings (z_I, z_E). Adapting from state-of-the-art generative techniques, our diffusion process is specifically conditioned on the EEG embedding z_E to adeptly capture the distribution of CLIP embeddings $p(z_I|z_E)$. The CLIP embedding z_I , procured during this phase, establishes the groundwork for the ensuing image generation stage. Our architecture incorporates a streamlined U-Net, labeled as $\epsilon_{\text{prior}}(z_I^t; t, z_E)$, where z_I^t signifies the perturbed CLIP embedding at a given diffusion timestep t . The training utilizes pairs from the ImageNet database, consisting of over a million images, to fine-tune the EEG-Conditioned Diffusion model. This model is meticulously trained using the classifier-free guidance approach, effectively balancing the conditioning signal's fidelity with the generative output's diversity.

Classifier-free guidance method The Classifier-Free Guidance technique is crucial in guiding the iterative refinement of a Diffusion Model (DM) under a specific EEG condition z_E . It achieves this by synchronizing the outputs of both a conditional and an unconditional model. The model's formulation, $\epsilon_{\text{prior}}^w(z_I^t; t, z_E)$, is as follows:

$$\epsilon_{\text{prior}}^w(z_I^t; t, z_E) = (1 + w)\epsilon_{\text{prior}}(z_I^t; t, z_E) - w\epsilon_{\text{prior}}(z_I^t; t), \tag{4}$$

where $w \geq 0$ represents the *guidance scale*. This mechanism facilitates concurrent training of the conditional and unconditional models within a singular network framework, periodically substituting the EEG embedding z_E with a null vector to promote training variability, i.e. 10% of the time. The primary objective of this method is to enhance the sample quality produced by DMs while maintaining output diversity.

C.2 Stage II - CLIP-Embedded Image Synthesis

In Fig. 11, we compare the effects of one-stage and two-stage EEG-guided image generation. We show images generated using EEG embeddings directly (**One-stage**) and images generated using image embeddings obtained via prior diffusion (**Two-stage**). It can be seen that the two-stage EEG-guided image generation can more accurately reconstruct the semantic and low-level visual features of the original image, and the style is more realistic.



Fig. 11. Comparison between one-stage and two-stage EEG guidance image generation. (a) We present the images that subjects seen (**Seen**), the generated images directly using EEG embeddings (**One-stage**), and the generated images from image embeddings obtained by the prior diffusion (**Two-stage**). These results indicate that the strategy of our two-stage generation can better reconstruct the seen visual stimuli. (b) We employed ATM-S to compare the generated images with the original images in a retrieval task. Our result indicates that the images generated in two stages significantly enhance the performance of the original model on the retrieval task.

In the second stage of our EEG-based image generation approach, the CLIP embedding z_I derived from the EEG-conditioned diffusion acts as the precursor for synthesizing visual objects I based on z_I . This is achieved by harnessing the synergies of advanced pre-trained models, namely SDXL and IP-Adapter [33, 59], facilitating the creation of high-caliber images.

The cornerstone of our synthesis process is the SDXL framework, acclaimed for its proficiency in text-to-image conversion. The integration of the IP-Adapter introduces dual cross-attention mechanisms, allowing the CLIP embedding z_I to serve as a directive input and guide the denoising trajectory within the U-Net structure. The synthesis model is denoted as $\epsilon_{\text{SD}}(z_t, t, z_I)$, where z_t denotes the SDXL Variational Autoencoder's (VAE) disturbed latents.

SDXL-turbo for accelerated processing To augment the efficiency of our framework, we additionally explore the SDXL-Turbo [36], a refined iteration of SDXL optimized for swift image synthesis. This variant proves especially beneficial in scenarios demanding quick generation of high-fidelity visuals.

IP-Adapter's efficacy The IP-Adapter, with its compact design, has proven to be effective in enhancing image prompt adaptability within pre-trained text-to-image models. Its compatibility with text prompts for multimodal image generation extends the versatility of our EEG-based image synthesis approach.

D Performance comparison

Comparison metrics Our study uses various metrics to evaluate how well we can recreate visual stimuli from brain data (EEG, MEG, fMRI) (Table 1 in main text). These metrics include SSIM (structural similarity index metric)[51], SwAV (SwAV-ResNet50, refer to average correlation distance)[5], and two-way identification using neural networks (AlexNet(2/5), Inception, CLIP. Here AlexNet(2/5) the 2nd and 5th feature layers of AlexNet) for both low-level and high-level image features. Here two-way identification can be seen as a two-way retrieval task described in Appendix B.1. In Tab. 3, our results showed that on the THINGS dataset, we could achieve performance over MEG on EEG reconstruction using ATM. Tab. 4 shows the

Table 3. Quantitative assessments of the reconstruction quality for EEG, MEG, and fMRI. For detailed explanations of the metrics.

Dataset \uparrow	Low-level			High-level		
	SSIM \uparrow	AlexNet(2) \uparrow	AlexNet(5) \uparrow	Inception \uparrow	CLIP \uparrow	SwAV \downarrow
NSD (B.D.) [4]	0.366	0.962	0.977	0.910	0.917	0.410
NSD (Brain-Diffuser) [31]	0.356	0.942	0.962	0.872	0.915	0.423
NSD (MindEye) [39]	0.308	0.917	0.974	0.936	0.942	0.369
THINGS-MEG (B.D.) [4]	0.327	0.695	0.753	0.593	0.700	0.630
THINGS-MEG (Ours)	0.340	0.613	0.672	0.619	0.603	0.651
THINGS-EEG (Ours)	0.345	0.776	0.866	0.734	0.786	0.582

decoding performance of different data sets (fMRI, MEG, EEG) on visual stimulus tasks, and we even achieved the same or better performance than fMRI and MEG. Our results suggest that a suitable upstream neural representation plays a decisive role in the downstream task.

Table 4. The classification performance of various methods are discussed. Due to differences in datasets and data modalities, we have specified unified metrics to objectively assess the performance of each method.

Dataset	Model	50-way		100-way		200-way	
		top-1	top-5	top-1	top-5	top-1	top-5
GOD-Wiki (fMRI)	CADA-VAE (V&T) [38]	10.02	40.37	-	-	-	-
	MVAE (V&T) [56]	10.04	39.60	-	-	-	-
	MMVAE (V&T) [43]	11.68	43.29	-	-	-	-
	MoPoE-VAE (V&T) [47]	12.90	51.78	-	-	-	-
	BraVL (V&T) [11]	13.99	53.13	-	-	-	-
THINGS (MEG)	ATM (Ours)	15.63	41.38	11.75	29.25	5.88	19.25
THINGS (EEG)	BraVL [11]	14.33	40.28	-	-	5.82	17.45
	ATM (Ours)	17.40	39.40	11.50	28.50	7.40	20.60

E Representational analysis

As depicted in Fig. 12, we showcase the representational similarity matrix and visualization in the latent space. To investigate the relationship between the representations obtained from EEG and those of images, we conducted a representational similarity matrix. We focused on subject 8, who exhibited the highest retrieval accuracy. By applying a clustering algorithm to the image embeddings corresponding to 200 images in the test set, we observed distinct within-category clustering. We generated similarity matrices based on both image and text embeddings, which were then compared with EEG representations. As shown in Fig. 12, clear within-category clustering is observable in the representational similarity matrix with image, whereas this phenomenon is not present in the representational similarity matrix with text.

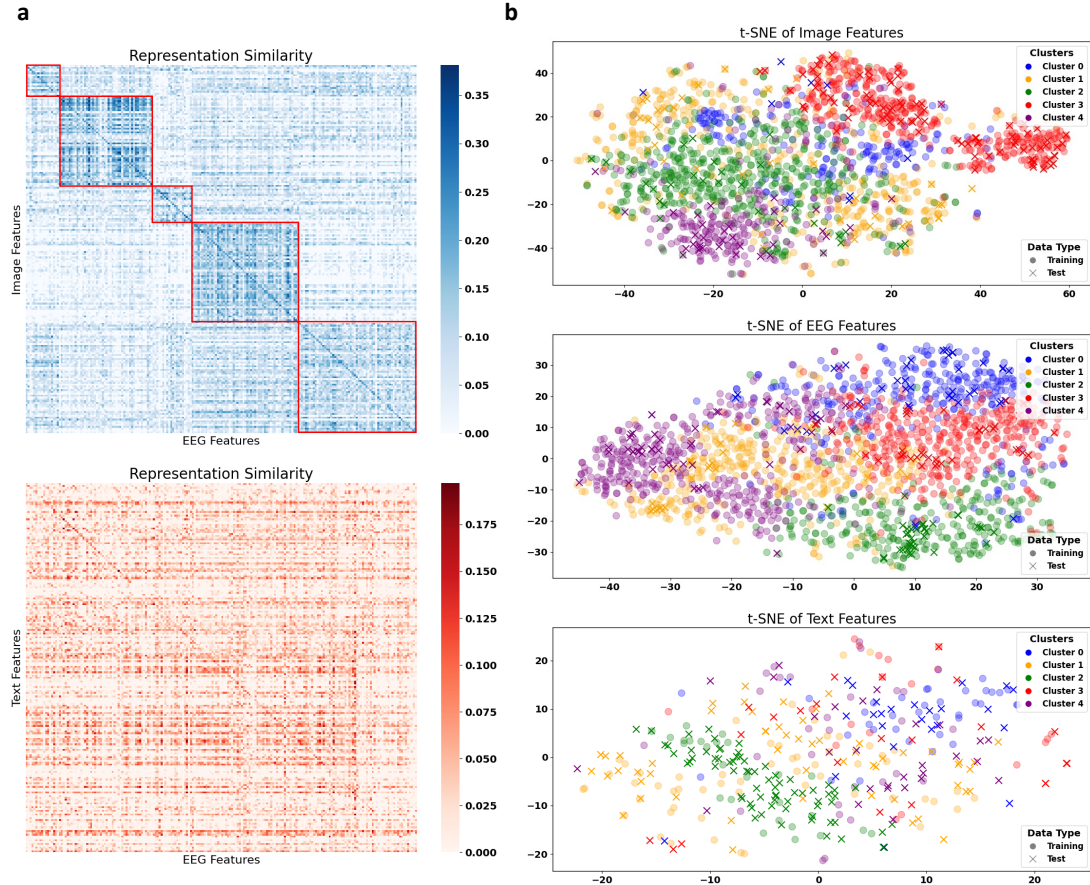


Fig. 12. Visualization of the representation of EEG, image and text modality. (a) Representational similarity matrix between EEG features and image/text features. (b) Visualization in the latent space of EEG/image/text by t-SNE.

F Additional images results

F.1 Additional retrieval results



Fig. 13. Additional retrieval results

F.2 Additional generated images

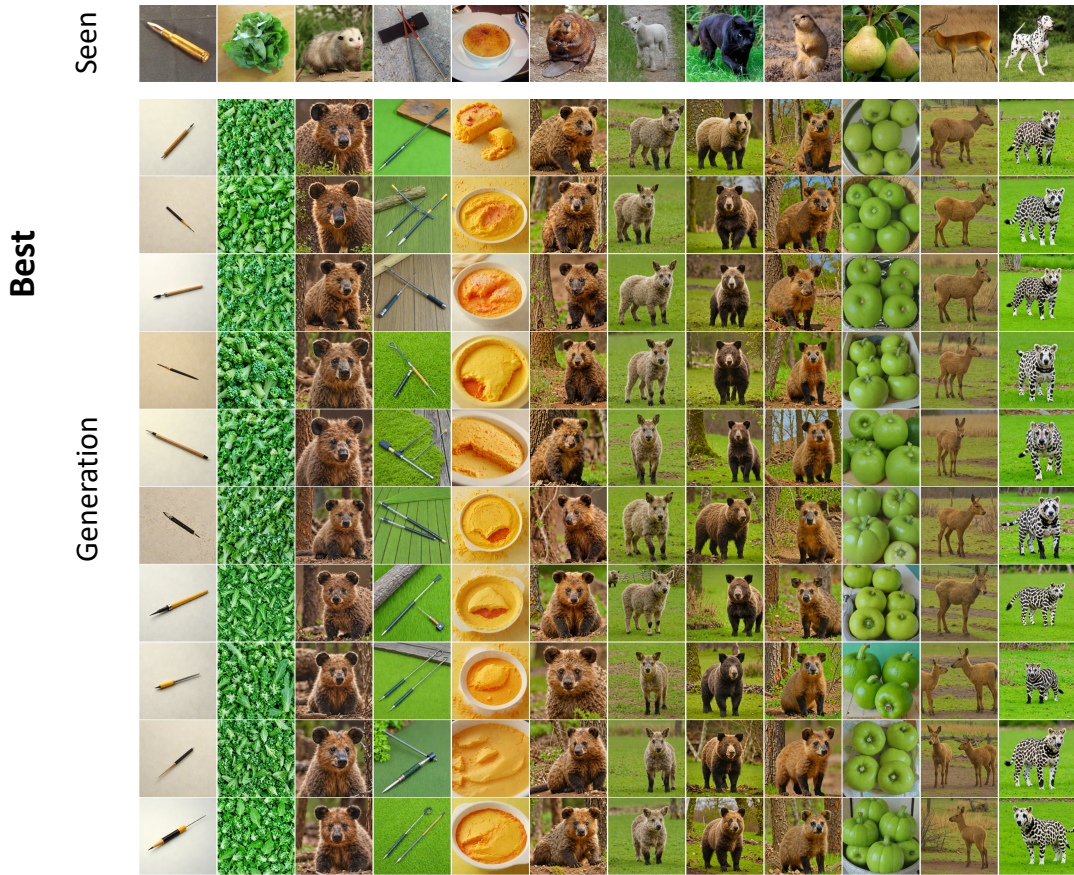


Fig. 14. Additional generated results with the best alignment to original images

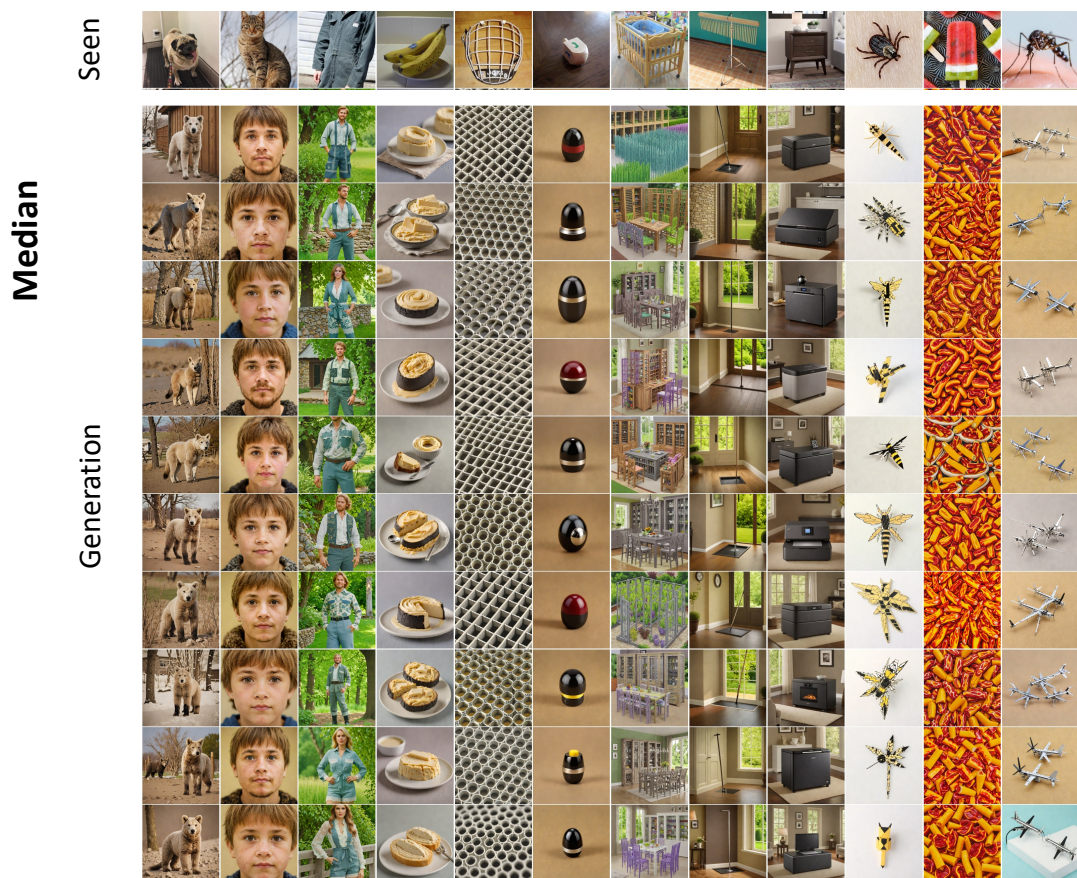


Fig. 15. Additional generated results with the median alignment to original images

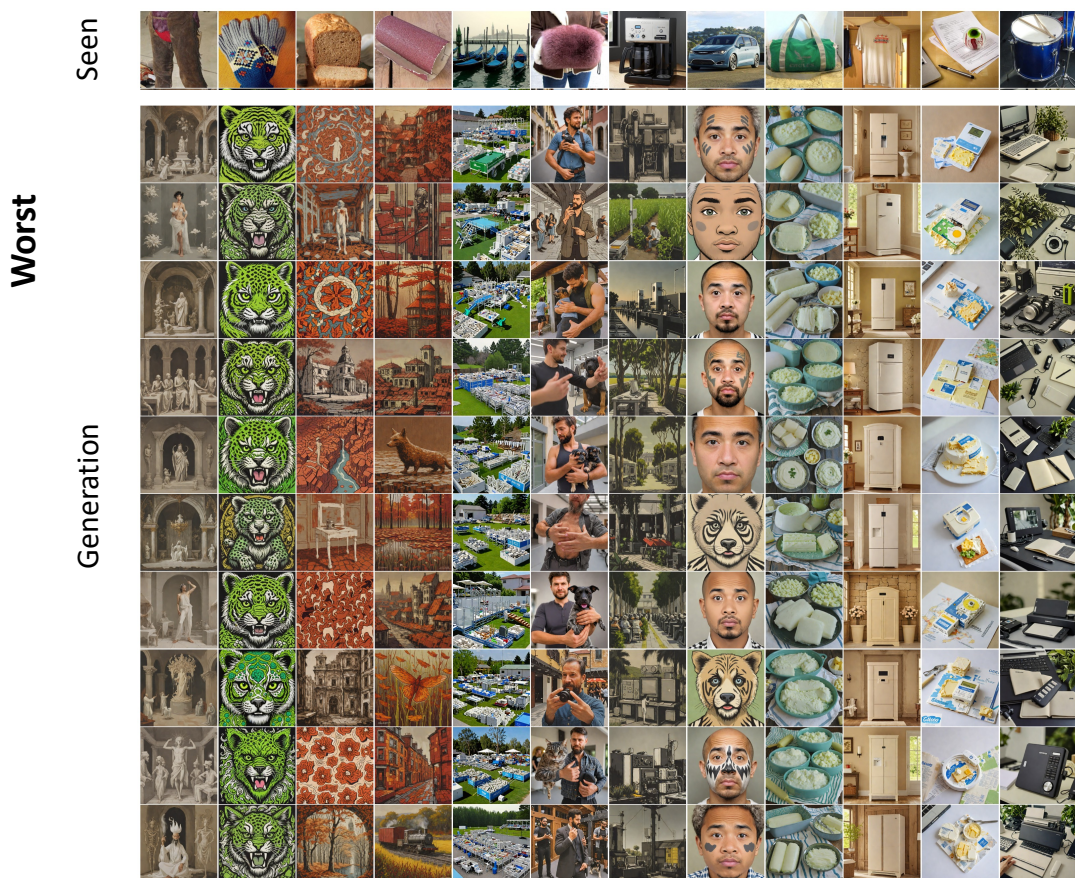


Fig. 16. Additional generated results with the worst alignment to original images

F.3 Additional generated images for each subject

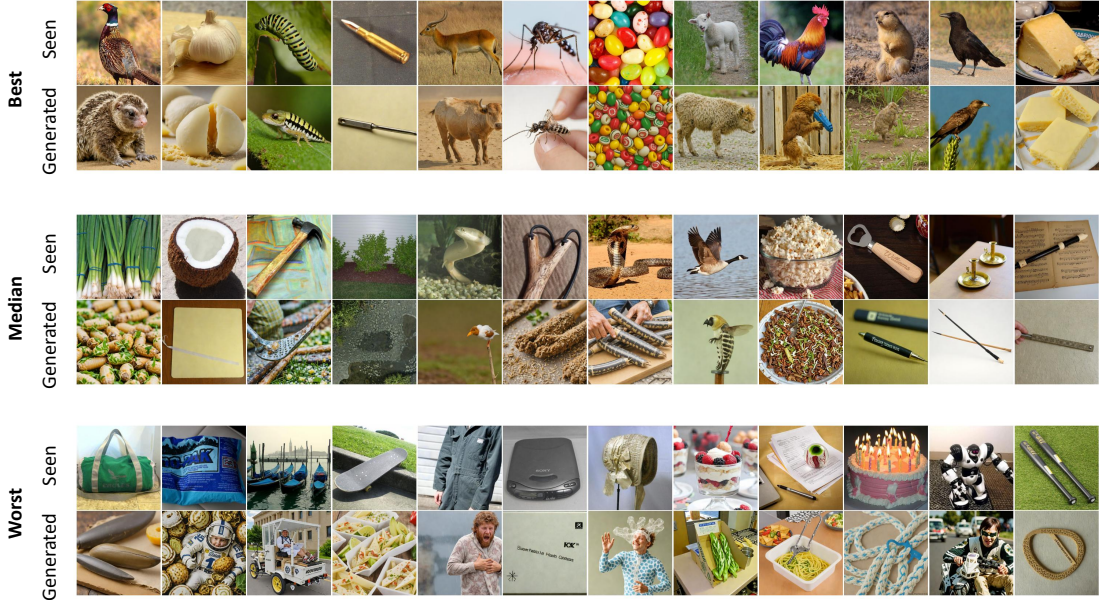


Fig. 17. Part of subject 1 generates images. We do a batch generation of the subjects and then calculate the best, medium, and worst performers compared to the original stimulus pictures.

G Additional evaluation results

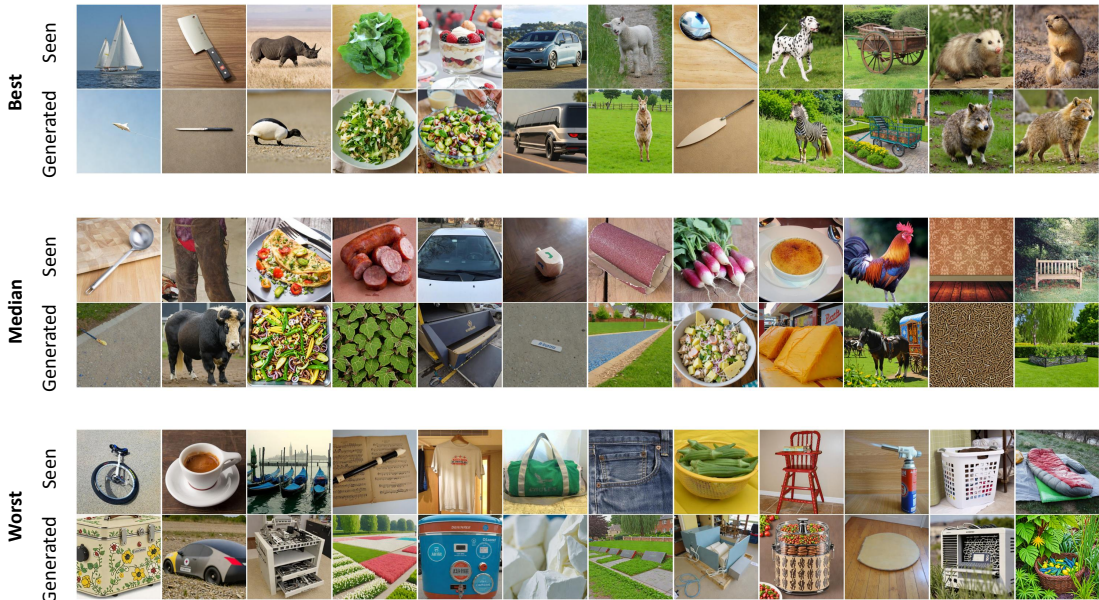


Fig. 18. Part of subject 2 generates images. We do a batch generation of the subjects and then calculate the best, medium, and worst performers compared to the original stimulus pictures.

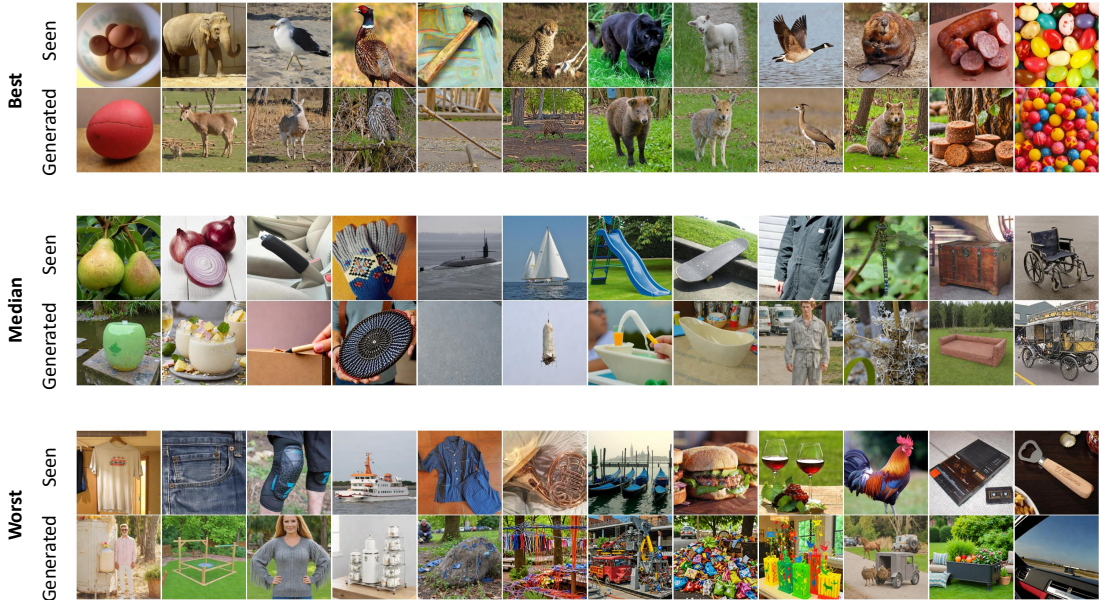


Fig. 19. Part of subject 3 generates images. We do a batch generation of the subjects and then calculate the best, medium, and worst performers compared to the original stimulus pictures.

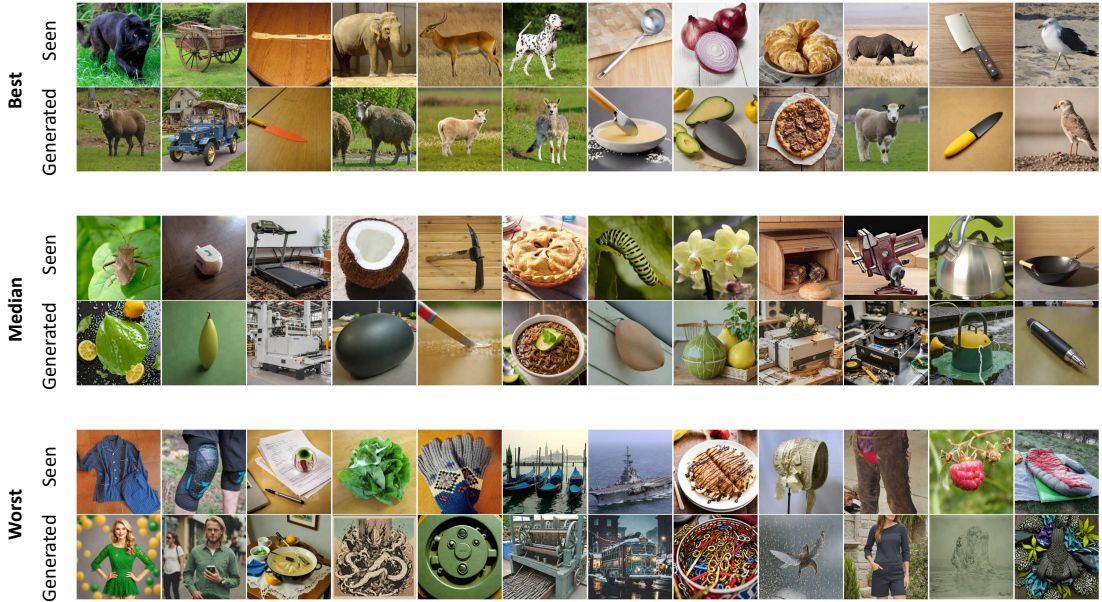


Fig. 20. Part of subject 4 generates images. We do a batch generation of the subjects and then calculate the best, medium, and worst performers compared to the original stimulus pictures.

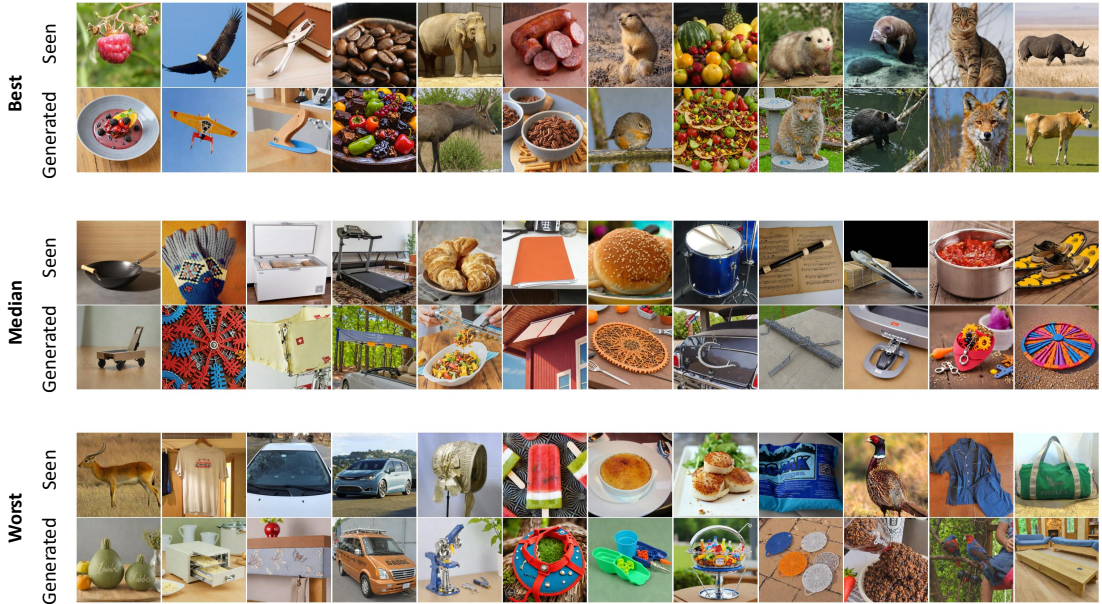


Fig. 21. Part of subject 5 generates images. We do a batch generation of the subjects and then calculate the best, medium, and worst performers compared to the original stimulus pictures.

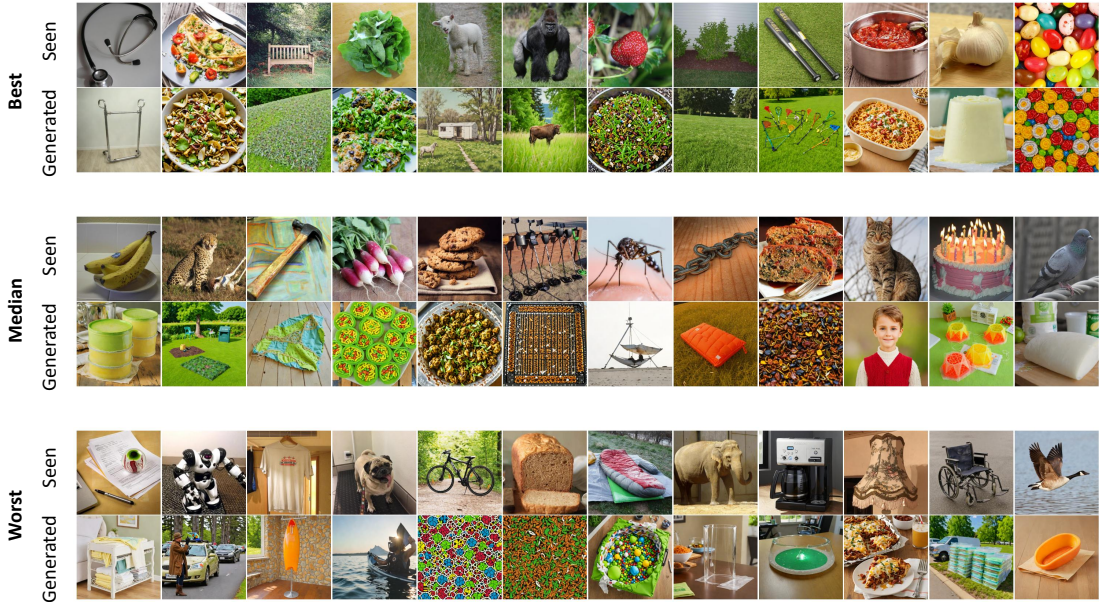


Fig. 22. Part of subject 6 generates images. We do a batch generation of the subjects and then calculate the best, medium, and worst performers compared to the original stimulus pictures.

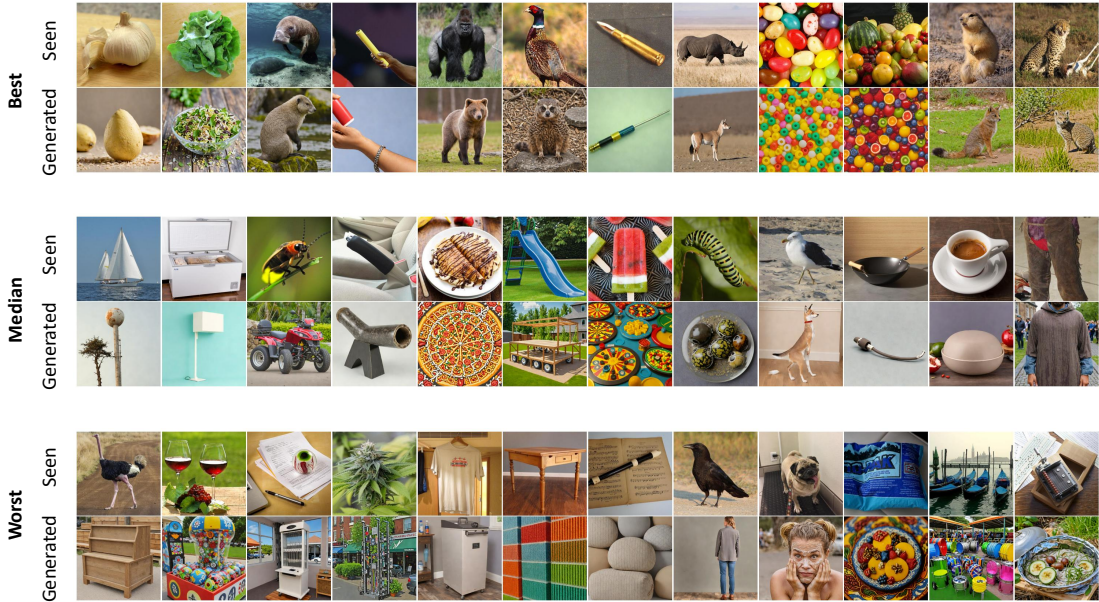


Fig. 23. Part of subject 7 generates images. We do a batch generation of the subjects and then calculate the best, medium, and worst performers compared to the original stimulus pictures.

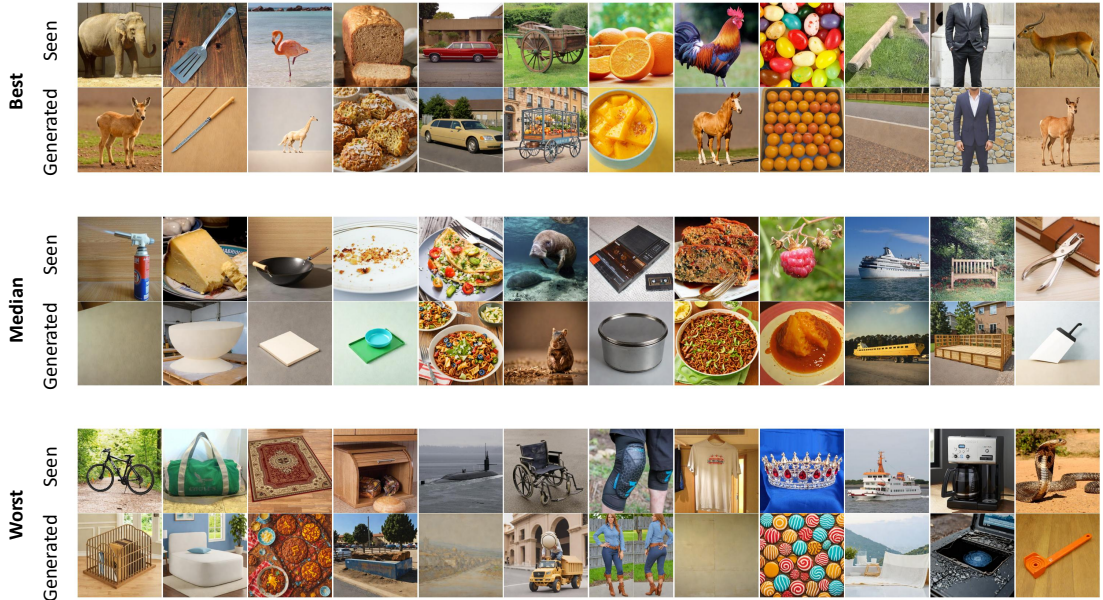


Fig. 24. Part of subject 8 generates images. We do a batch generation of the subjects and then calculate the best, medium, and worst performers compared to the original stimulus pictures.

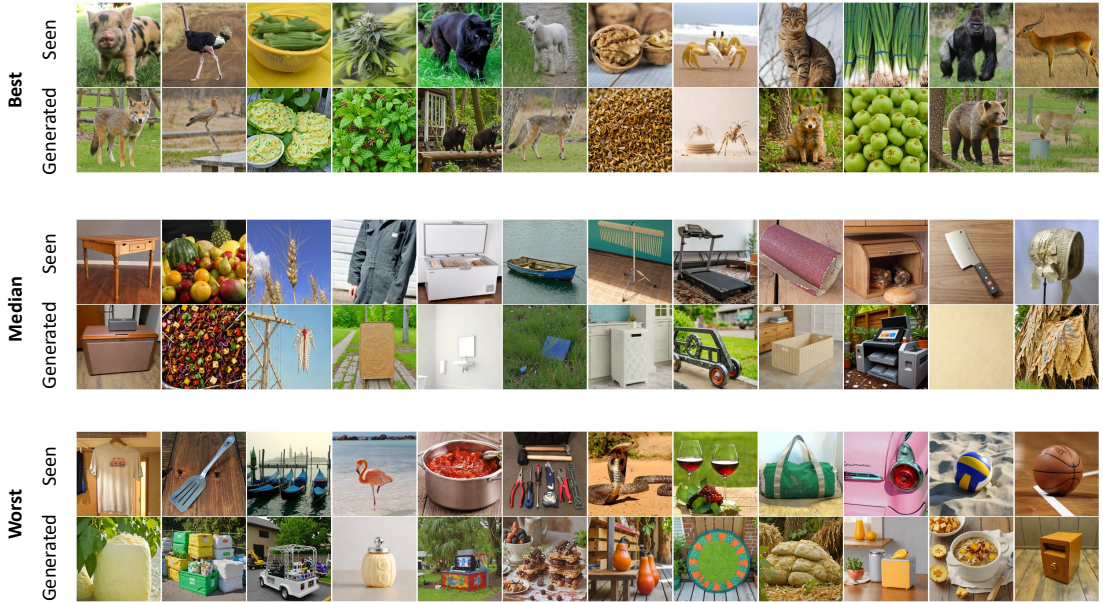


Fig. 25. Part of subject 9 generates images. We do a batch generation of the subjects and then calculate the best, medium, and worst performers compared to the original stimulus pictures.



Fig. 26. Part of subject 10 generates images. We do a batch generation of the subjects and then calculate the best, medium, and worst performers compared to the original stimulus pictures.

G.1 Accuracy for time windows

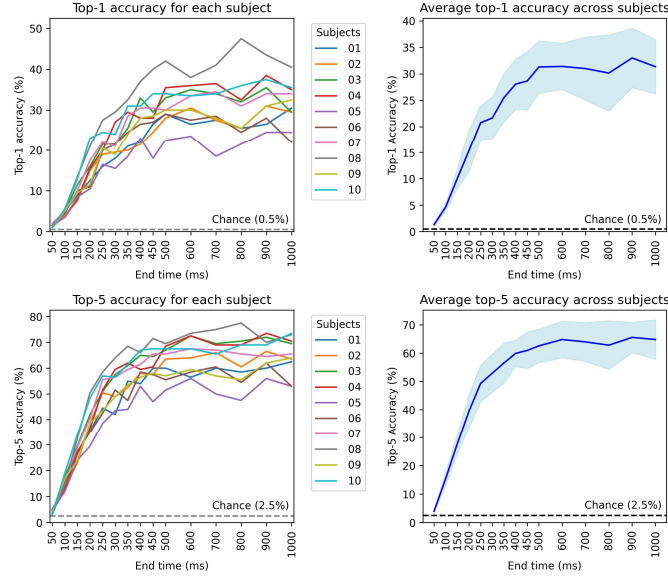


Fig. 27. Accuracy for growing windows. We use an EEG time window of 100ms, sliding 100ms each time. (a) Top-1 accuracy. (b) Top-5 accuracy.

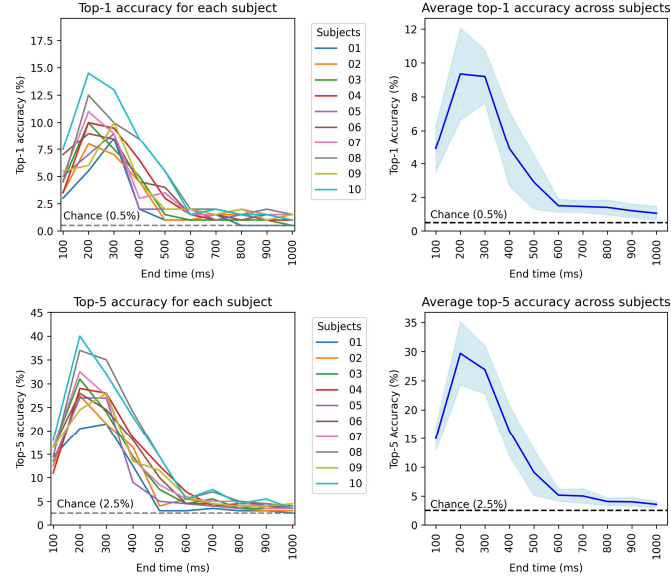


Fig. 28. Accuracy for sliding windows. We use an EEG time window of 100ms, sliding 100ms each time. (a) Top-1 accuracy. (b) Top-5 accuracy.

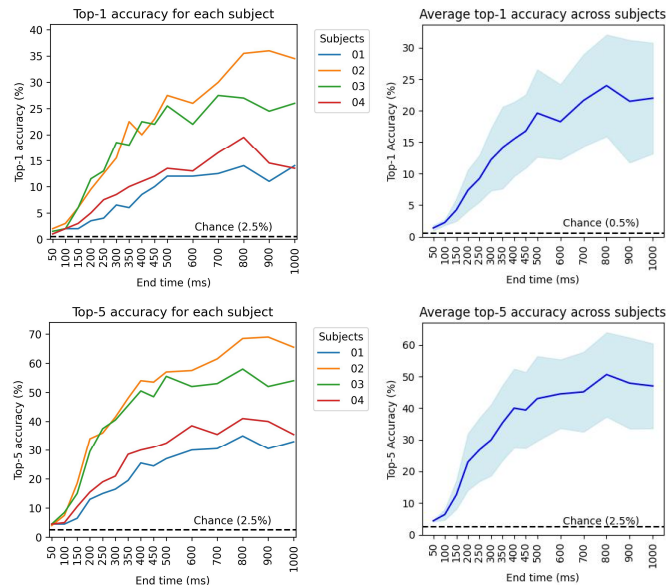


Fig. 29. Accuracy for growing windows. The MEG time window grows from 50ms to 1000ms. (a) Top-1 accuracy. (b) Top-5 accuracy.

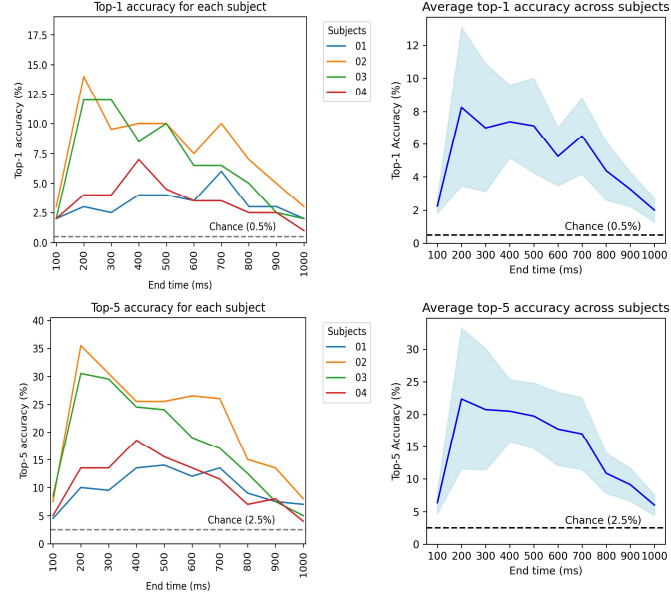


Fig. 30. Accuracy for sliding windows. We use an MEG time window of 100ms, sliding 100ms each time. (a) Top-1 accuracy. (b) Top-5 accuracy.

Table 5. Overall accuracy of zero-shot retrieval on **THINGS-EEG** dataset. We showed in-subject and cross-subject retrieval task performance (Ave \pm Std.%) under the condition of **batch size=16**. We compared the 2-way, 4-way, 10-way, the Top-1 and Top-5 accuracy of 200-way from different EEG embedding methods. Our ATM outperformed all the others.

Subject dependent - train and test on one subject (batch size=16)					
Methods	2-Way	4-Way	10-Way	Top-1	Top-5
EEGITNet	83.23 \pm 2.77	65.67 \pm 3.84	43.87 \pm 3.78	7.79 \pm 1.27	22.12 \pm 2.88
EEGConformer	89.18 \pm 2.88	75.49 \pm 5.30	55.32 \pm 6.88	11.29 \pm 3.55	33.49 \pm 6.78
ShallowFBCSPNet	84.29 \pm 2.56	67.13 \pm 3.61	46.07 \pm 4.55	8.26 \pm 2.95	25.87 \pm 5.03
EEGNetV4	89.03 \pm 2.86	75.40 \pm 5.18	56.77 \pm 6.60	13.29 \pm 3.99	35.50 \pm 7.14
B.D.	91.14 \pm 2.45	79.59 \pm 4.59	62.62 \pm 6.33	16.29 \pm 4.35	42.16 \pm 7.56
NICE	92.17 \pm 2.78	82.10 \pm 5.55	65.65 \pm 8.03	19.40 \pm 5.83	46.26 \pm 10.42
MLP	87.67 \pm 4.41	72.55 \pm 7.62	53.52 \pm 9.45	11.81 \pm 4.33	32.74 \pm 9.24
ATM-S (Ours)	93.89 \pm 1.97	85.38 \pm 3.95	71.63 \pm 6.17	22.84 \pm 5.87	52.22 \pm 8.34
ATM-E (Ours)	94.44 \pm 1.76	86.11 \pm 3.39	71.89 \pm 5.64	24.38 \pm 6.56	54.14 \pm 8.08

Subject independent - leave one subject for test (batch size=16)					
Methods	2-Way	4-Way	10-Way	Top-1	Top-5
EEGITNet	77.14 \pm 4.14	55.29 \pm 6.22	31.88 \pm 6.20	2.93 \pm 1.70	13.00 \pm 4.45
EEGConformer	79.49 \pm 3.91	59.31 \pm 5.83	36.67 \pm 5.35	4.11 \pm 1.83	17.04 \pm 4.21
ShallowFBCSPNet	75.14 \pm 4.45	53.06 \pm 6.70	31.23 \pm 6.56	3.19 \pm 2.17	13.01 \pm 5.15
EEGNetV4	82.60 \pm 3.17	64.28 \pm 5.44	42.24 \pm 6.10	6.13 \pm 2.40	21.23 \pm 5.19
B.D.	81.49 \pm 3.52	62.35 \pm 6.44	40.53 \pm 7.19	6.16 \pm 2.40	20.45 \pm 5.40
NICE	81.85 \pm 2.53	63.57 \pm 4.46	41.86 \pm 4.68	6.43 \pm 1.46	21.39 \pm 3.62
MLP	80.49 \pm 2.61	62.09 \pm 3.88	40.37 \pm 3.71	5.67 \pm 1.09	19.97 \pm 3.02
ATM-S (Ours)	82.88 \pm 5.18	65.03 \pm 8.51	44.86 \pm 9.85	8.04 \pm 3.34	24.62 \pm 8.17
ATM-E (Ours)	83.30 \pm 3.92	65.80 \pm 6.98	44.84 \pm 7.76	7.47 \pm 2.84	23.75 \pm 6.86

Table 6. Overall accuracy of zero-shot Retrieval on **THINGS-EEG** dataset. We showed in-subject and cross-subject retrieval task performance (Ave \pm Std.%) under the condition of **batch size=1024**. We compared the 2-way, 4-way, 10-way, the Top-1 and Top-5 accuracy of 200-way from different EEG embedding methods. Our ATM outperformed all the others.

Subject dependent - train and test on one subject (batch size=1024)						
Methods	2-Way	4-Way	10-Way	Top-1	Top-5	
EEGNet	76.69 \pm 12.97	56.99 \pm 16.31	36.35 \pm 15.11	5.75 \pm 3.62	18.14 \pm 9.40	
EEGConformer	76.17 \pm 13.13	56.29 \pm 16.70	34.72 \pm 14.79	3.98 \pm 2.80	17.10 \pm 9.21	
ShallowFBCSPNet	74.32 \pm 12.14	53.97 \pm 15.81	33.48 \pm 14.35	6.10 \pm 4.61	16.53 \pm 9.94	
EEGNetV4	92.81 \pm 2.22	83.15 \pm 4.20	67.81 \pm 6.11	19.51 \pm 5.19	48.99 \pm 6.75	
B.D.	78.42 \pm 8.81	58.24 \pm 12.13	37.97 \pm 11.38	5.88 \pm 3.49	18.61 \pm 7.81	
NICE	92.73 \pm 2.75	83.26 \pm 5.47	67.96 \pm 8.31	19.32 \pm 5.33	49.26 \pm 9.69	
MLP	83.09 \pm 2.54	66.70 \pm 4.16	45.43 \pm 4.58	7.23 \pm 1.66	25.14 \pm 3.66	
ATM-S (Ours)	94.60 \pm 1.93	86.88 \pm 4.20	73.89 \pm 5.93	26.09 \pm 6.96	58.07 \pm 8.16	
ATM-E (Ours)	92.99 \pm 2.20	83.81 \pm 4.46	68.87 \pm 7.27	22.40 \pm 6.62	50.59 \pm 9.59	
Subject independent - leave one subject for test (batch size=1024)						
Methods	2-Way	4-Way	10-Way	Top-1	Top-5	
EEGNet	77.47 \pm 3.75	55.75 \pm 6.01	33.60 \pm 6.16	3.80 \pm 2.01	14.02 \pm 3.89	
EEGConformer	68.02 \pm 7.75	44.24 \pm 9.25	23.84 \pm 7.65	1.66 \pm 1.37	8.62 \pm 4.20	
ShallowFBCSPNet	76.40 \pm 4.64	54.81 \pm 7.09	32.37 \pm 7.28	2.49 \pm 1.57	13.24 \pm 5.98	
EEGNetV4	82.60 \pm 3.17	64.28 \pm 5.44	42.24 \pm 6.10	6.13 \pm 2.40	21.23 \pm 5.19	
B.D.	85.30 \pm 6.24	69.87 \pm 10.09	50.82 \pm 11.74	10.57 \pm 5.26	29.74 \pm 11.28	
NICE	83.75 \pm 3.21	65.82 \pm 5.93	44.41 \pm 6.12	7.04 \pm 2.83	23.55 \pm 4.86	
MLP	80.49 \pm 2.61	62.09 \pm 3.88	40.37 \pm 3.71	5.67 \pm 1.09	19.97 \pm 3.02	
ATM-S (Ours)	87.36 \pm 3.97	72.80 \pm 7.02	53.80 \pm 8.41	11.84 \pm 4.80	33.73 \pm 8.73	
ATM-E (Ours)	87.41 \pm 3.07	72.85 \pm 5.51	53.15 \pm 6.52	11.12 \pm 3.26	32.61 \pm 6.78	

Table 7. Accuracy of zero-shot Retrieval on **THINGS-EEG** for odd-numbered subjects(batch size=16).

Subject dependent - train and test on one subject (batch size=16)										
Method	Subject 1		Subject 3		Subject 5		Subject 7		Subject 9	
	top-1	top-5								
EEGNet	8.20	19.45	6.95	24.25	6.30	19.50	8.95	19.00	6.10	21.60
Conformer	4.75	21.30	9.90	34.15	7.55	28.05	12.25	35.35	13.95	34.10
ShallowFBCSPNet	7.00	20.90	8.45	28.45	7.75	20.80	6.35	27.60	2.80	18.00
EEGNetV4	10.85	31.10	17.65	41.20	6.75	21.80	14.15	39.05	10.40	30.50
B.D.	13.05	36.00	14.45	37.85	10.55	32.00	18.65	46.80	14.60	37.55
NICE	13.25	35.75	23.15	51.40	12.40	33.45	19.45	50.20	17.55	41.70
MLP	13.00	38.30	13.90	39.60	8.00	24.85	13.00	39.15	12.65	36.20
ATM-S (Ours)	19.10	49.05	22.95	56.30	16.10	39.95	25.75	55.40	21.50	48.15
ATM-E (Ours)	20.75	47.35	25.10	56.45	18.50	44.35	24.70	54.10	23.40	52.40
Subject independent - leave one subject for test (batch size=16)										
Method	Subject 1		Subject 3		Subject 5		Subject 7		Subject 9	
	top-1	top-5								
EEGNet	3.40	13.75	1.05	10.80	1.45	7.55	4.30	13.65	0.55	5.95
Conformer	5.45	20.10	2.00	12.75	2.90	12.95	5.50	16.45	1.05	9.90
ShallowFBCSPNet	4.25	13.30	1.45	7.65	0.90	7.40	3.75	13.75	0.65	5.95
EEGNetV4	7.20	22.40	4.60	17.80	3.00	15.75	3.80	18.95	3.40	12.70
B.D.	6.55	21.45	5.45	17.00	3.10	14.75	6.45	24.00	2.60	12.75
NICE	4.80	20.05	5.80	18.10	5.85	16.95	5.75	21.20	4.95	17.65
MLP	3.65	16.20	5.95	20.95	5.90	19.20	4.40	14.25	7.45	23.85
ATM-S (Ours)	8.30	25.50	11.40	31.30	5.95	21.25	4.80	19.45	4.05	13.30
ATM-E (Ours)	7.80	22.95	13.75	35.70	4.20	14.30	6.40	25.95	4.50	14.90

Table 8. Accuracy of zero-shot Retrieval on **THINGS-EEG** for even-numbered subjects(batch size=16).

Method	Subject dependent - train and test on one subject (batch size=16)											
	Subject 2		Subject 4		Subject 6		Subject 8		Subject 10		Overall	Avg
	top-1	top-5	top-1	top-5	top-1	top-5	top-1	top-5	top-1	top-5	top-1	top-5
EEGNet	6.55	19.05	7.90	23.10	8.10	23.10	9.80	27.35	9.05	24.85	8.08	23.49
Conformer	8.10	25.80	13.30	37.10	12.75	36.65	15.75	45.10	14.55	37.35	12.89	36.40
ShallowFBCSPNet	6.15	23.50	10.85	29.10	9.05	26.95	13.15	34.90	11.00	28.55	10.04	28.60
EEGNetV4	8.80	28.20	14.30	37.45	15.40	42.45	19.40	42.40	15.15	40.85	14.61	38.27
B.D.	13.35	38.00	17.45	45.00	14.25	40.35	24.50	54.65	22.10	53.45	18.33	46.29
NICE	11.45	31.05	20.75	48.95	22.25	50.35	29.75	62.40	24.00	57.40	21.64	50.03
MLP	10.85	33.10	15.20	37.70	12.15	35.05	18.65	47.55	18.30	45.55	15.03	39.79
ATM-S (Ours)	15.10	41.00	25.75	55.75	20.05	50.10	34.90	67.50	27.15	58.95	24.59	54.66
ATM-E (Ours)	15.25	44.90	25.75	55.75	23.00	53.95	39.40	70.25	29.60	63.75	26.26	57.36
Subject independent - leave one subject for test (batch size=16)												
Method	Subject 2		Subject 4		Subject 6		Subject 8		Subject 10		Overall	Avg
	top-1	top-5	top-1	top-5	top-1	top-5	top-1	top-5	top-1	top-5	top-1	top-5
EEGNet	2.65	11.40	3.25	15.35	8.10	23.10	9.80	27.35	9.05	24.85	6.57	20.41
Conformer	4.65	18.70	4.25	19.60	12.75	36.65	15.75	45.10	14.55	37.35	10.39	31.48
ShallowFBCSPNet	2.75	13.70	5.55	15.45	9.05	26.95	13.15	34.90	11.00	28.55	8.30	23.91
EEGNetV4	7.80	24.30	7.35	23.90	15.40	42.45	19.40	42.40	15.15	40.85	13.02	34.78
B.D.	5.00	16.40	6.65	22.35	14.25	40.35	24.50	54.65	22.10	53.45	14.50	37.44
NICE	5.55	21.40	8.20	24.90	22.25	50.35	29.75	62.40	24.00	57.40	17.95	43.29
MLP	5.50	20.65	5.45	18.35	12.15	35.05	18.65	47.55	18.30	45.55	12.01	33.43
ATM-S (Ours)	7.25	23.65	14.55	39.80	20.05	50.10	34.90	67.50	27.15	58.95	20.78	47.90
ATM-E (Ours)	8.65	27.60	14.55	39.80	23.00	53.95	39.40	70.25	29.60	63.75	21.62	47.93

Table 9. Accuracy of zero-shot Retrieval on **THINGS-EEG** for odd-numbered subjects(batch size=1024).

Method	Subject dependent - train and test on one subject (batch size=1024)									
	Subject 1		Subject 3		Subject 5		Subject 7		Subject 9	
	Top-1	Top-5	Top-1	Top-5	Top-1	Top-5	Top-1	Top-5	Top-1	Top-5
EEGNet	0.50	3.45	2.40	7.75	5.35	18.25	8.90	24.90	5.50	22.45
Conformer	0.50	3.20	0.50	6.90	3.40	17.50	7.10	23.80	6.15	22.75
ShallowFBCSPNet	0.65	3.35	2.30	6.20	3.35	14.55	7.35	23.15	6.80	18.05
EEGNetV4	11.45	41.45	20.85	48.70	13.75	42.00	19.05	50.30	15.50	40.60
B.D.	6.70	23.25	6.70	19.75	1.70	8.10	5.85	20.55	6.80	21.05
NICE	17.65	50.25	22.05	51.20	9.80	27.65	17.15	49.60	19.60	52.55
MLP	8.40	24.40	5.60	22.65	6.00	25.15	8.35	24.35	5.45	22.25
ATM-S (Ours)	25.60	60.40	25.00	62.35	12.90	43.00	30.50	61.50	24.35	51.50
ATM-E (Ours)	18.85	44.10	24.30	56.10	11.95	32.65	24.85	53.75	20.05	47.75
Subject independent - leave one subject for test (batch size=1024)										
Method	Subject 1		Subject 3		Subject 5		Subject 7		Subject 9	
	Top-1	Top-5	Top-1	Top-5	Top-1	Top-5	Top-1	Top-5	Top-1	Top-5
EEGNet	4.45	13.95	1.50	12.05	1.00	8.60	4.50	13.35	1.00	8.95
Conformer	4.45	17.20	0.70	4.75	0.50	5.30	2.40	10.95	0.50	3.35
ShallowFBCSPNet	2.00	11.25	1.70	9.25	1.00	4.85	3.80	17.30	1.00	5.75
EEGNetV4	9.45	24.00	8.20	21.90	5.20	18.75	5.45	21.80	5.65	16.40
B.D.	5.30	16.60	13.45	35.30	8.15	21.30	15.85	37.75	8.10	27.10
NICE	4.80	20.05	6.75	20.70	4.15	18.55	5.55	24.45	5.10	17.20
MLP	4.45	12.30	6.75	24.60	4.90	19.55	4.85	17.60	4.45	19.80
ATM-S (Ours)	10.45	26.75	11.85	33.80	6.95	23.85	16.05	43.50	4.85	22.70
ATM-E (Ours)	10.45	26.75	13.45	35.30	8.15	24.75	15.85	39.05	7.55	30.65

Table 10. Accuracy of zero-shot Retrieval on **THINGS-EEG** for even-numbered subjects(batch size=1024).

Method	Subject dependent - train and test on one subject (batch size=1024)										Overall Avg	
	Subject 2		Subject 4		Subject 6		Subject 8		Subject 10			
Top-1	Top-5	Top-1	Top-5	Top-1	Top-5	Top-1	Top-5	Top-1	Top-5	Top-1	Top-5	Top-1
EEGITNet	0.75	5.55	6.00	20.35	7.60	20.80	10.55	28.00	9.90	29.95	7.16	20.93
Conformer	0.50	3.70	3.30	18.10	4.35	21.95	7.50	25.00	6.50	28.15	4.43	19.38
ShallowFBCSPNet	0.75	4.75	5.25	16.35	7.80	16.95	13.45	32.20	13.25	29.70	8.10	20.19
EEGNetV4	17.30	43.60	27.20	58.75	20.55	53.25	22.95	56.45	26.50	54.85	22.90	53.38
B.D.	1.55	6.90	3.65	15.30	3.55	13.05	9.65	27.00	12.70	31.15	6.22	18.68
NICE	14.35	40.00	20.00	49.90	18.35	49.75	28.05	62.65	26.25	59.10	21.40	52.28
MLP	6.40	19.45	7.35	27.50	6.75	25.40	7.00	27.20	10.95	33.05	7.69	26.52
ATM-S (Ours)	22.00	54.50	31.35	60.90	21.30	51.05	38.80	72.00	29.05	63.50	28.50	60.39
ATM-E (Ours)	17.00	44.85	23.00	51.25	19.40	47.55	35.65	66.75	29.00	61.15	24.81	54.31

Method	Subject independent - leave one subject for test (batch size=1024)										Overall Avg	
	Subject 2		Subject 4		Subject 6		Subject 8		Subject 10			
Top-1	Top-5	Top-1	Top-5	Top-1	Top-5	Top-1	Top-5	Top-1	Top-5	Top-1	Top-5	Top-1
EEGITNet	4.70	15.20	4.80	14.40	5.50	17.45	3.70	14.25	6.90	22.00	5.12	16.66
Conformer	1.40	9.70	1.15	8.20	1.15	9.70	0.80	5.15	3.55	11.95	1.61	8.94
ShallowFBCSPNet	2.50	12.15	2.60	17.20	2.15	16.95	1.80	13.15	6.30	24.55	3.07	16.80
EEGNetV4	8.25	28.15	9.45	26.05	6.40	24.60	9.20	23.60	10.15	36.95	8.69	27.87
B.D.	4.45	23.20	4.30	12.90	11.15	33.70	18.05	46.30	16.90	43.30	10.97	31.88
NICE	4.90	22.80	9.65	29.70	8.35	24.35	7.90	25.00	13.25	32.75	8.81	26.92
MLP	6.50	21.55	9.50	25.15	3.60	16.15	7.25	29.25	12.80	34.35	7.93	25.29
ATM-S (Ours)	7.10	24.75	14.65	39.40	11.10	35.80	14.95	40.25	20.45	46.50	13.65	37.34
ATM-E (Ours)	10.45	27.75	14.65	35.25	10.35	35.20	13.95	38.60	15.85	42.85	13.05	35.93